

Research Article

Controls of the Lithospheric Thermal Field of an Ocean-Continent Subduction Zone: The Southern Central Andes

C. Rodriguez Picada ^{1,2} M. Scheck-Wenderoth ^{1,3} J. Bott ¹ M. L. Gomez Dacal,¹
M. Cacace ¹ M. Pons ^{1,2} C. B. Prezzi ⁴ and M. R. Strecker ¹

¹HelmholtzZentrum GFZ-German Research Centre for Geosciences, Potsdam, Germany

²University of Potsdam, Institute of Geosciences, Potsdam, Germany

³RWTH Aachen University, Aachen, Germany

⁴IGEBA-(UBA-CONICET) Facultad de Ciencias Exactas y Naturales, Universidad de Buenos Aires, Buenos Aires, Argentina

Correspondence should be addressed to C. Rodriguez Picada; piceda@gfz-potsdam.de

Received 25 October 2021; Accepted 31 March 2022; Published 13 May 2022

Academic Editor: Matt Balme

Copyright © 2022 C. Rodriguez Picada et al. Exclusive Licensee GeoScienceWorld. Distributed under a Creative Commons Attribution License (CC BY 4.0).

In an ocean-continent subduction zone, the assessment of the lithospheric thermal state is essential to determine the controls of the deformation within the upper plate and the dip angle of the subducting lithosphere. In this study, we evaluate the degree of influence of both the configuration of the upper plate (i.e., thickness and composition of the rock units) and variations of the subduction angle on the lithospheric thermal field of the southern Central Andes (29°–39°S). Here, the subduction angle increases from subhorizontal (5°) north of 33°S to steep (~30°) in the south. We derived the 3D temperature and heat flow distribution of the lithosphere in the southern Central Andes considering conversion of *S* wave tomography to temperatures together with steady-state conductive thermal modeling. We found that the orogen is overall warmer than the forearc and the foreland and that the lithosphere of the northern part of the foreland appears colder than its southern counterpart. Sedimentary blanketing and the thickness of the radiogenic crust exert the main control on the shallow thermal field (<50 km depth). Specific conditions are present where the oceanic slab is relatively shallow (<85 km depth) and the radiogenic crust is thin. This configuration results in relatively colder temperatures compared to regions where the radiogenic crust is thick and the slab is steep. At depths >50 km, the temperatures of the overriding plate are mainly controlled by the mantle heat input and the subduction angle. The thermal field of the upper plate likely preserves the flat subduction angle and influences the spatial distribution of shortening.

1. Introduction

Temperature exerts a first-order control on the rheology of the lithosphere, affecting the depth of the brittle-ductile transition zone and the occurrence of thermally activated creep processes [1, 2]. In an active ocean-continent convergent plate-boundary system, the assessment of the temperature distribution within the lithosphere is crucial for understanding the mechanisms controlling subduction geometry (e.g., slab dip and subduction-zone curvature) and the localization of deformation within the upper plate, including the vergence of thrust belts [3–8]. Estimating the thermal state of the system is challenging, however, as it requires deciphering the complex and continuous interplay

between different heat transport mechanisms (conduction and convection) and heat sources. These across-scales phenomena include heat conduction, advection of the oceanic plate that steadily supplies colder material, variations of thermal properties within the plates (radiogenic heat production and thermal conductivity), frictional heating along the subduction interface, latent heat due to mineralogical phase transformations within the oceanic plate, and adiabatic heating in the asthenosphere (for a review, see [9, 10]).

Many modeling studies [11–15] have considered the temperature distribution of the lithosphere as the main driver of the dynamics of a subduction system. These studies adopted a simplified configuration of the upper plate in terms of its thickness and rock composition [14]. However,

the continental lithosphere is the product of a complex tectonic and magmatic history, involving terrane amalgamation, trench erosion, crustal thickening during subduction and collision, and extensional overprinting either during the final stages of orogeny or from deep-seated processes in the mantle [16, 17]. To address these considerations, other modeling studies have effectively shown how the present-day thermal field varies with respect to thickness and compositional heterogeneities within the lithosphere [18–23] and how these variations ultimately affect the long-term rheology of the lithospheric plate [5, 23–25].

The southern Central Andes (SCA, 27°–40°S, Figure 1) are a suitable region for studying the effect of both a heterogeneous configuration of the upper plate and differences in subduction geometry on the lithospheric thermal field in an ocean-continent convergent plate-boundary system for several reasons. Bordering the convergent margin between the oceanic Nazca Plate and the continental South American Plate, the SCA encompass several morphotectonic provinces, each characterized by a distinct pre-Cenozoic geological history and lithospheric configuration [26, 27]. These differences are rooted in complex tectonic and magmatic episodes of shortening and extension that span from the Neoproterozoic to the Quaternary [26, 28–35]. Major pulses of Andean deformation are thought to have occurred during the Late Cretaceous and Miocene [36, 37], when the style of deformation was significantly influenced not only by the characteristics of the subducting plate [38–40], but also by the reactivation of inherited tectonic heterogeneities, which influenced Cenozoic phases of erosion, sedimentation, and geomorphic evolution [41]. The SCA are subdivided into four first-order morphotectonic provinces: the forearc, the magmatic arc, the back-arc, and the foreland (Figure 1; [3, 26, 42]). These extensive regions are in turn subdivided into morphotectonic provinces that are characterized by distinct structural and geomorphic features. For the purposes of this study, we have defined as the Andean orogen only the magmatic arc and backarc provinces of Principal and Frontal Cordilleras, and thus not included the fold-and-thrust belt of the Precordillera and the Payenia volcanic province. The main features of the foreland are the reverse-fault-bounded basement uplifts of the Sierras Pampeanas and the Neuquén and Cuyo basins (Figure 1).

A distinct feature of the SCA is the variation in the subduction angle along the strike of the subduction zone, transitioning between 33°S and 34.5°S from subhorizontal (<5°) in the north (Chilean-Pampean flat-slab area; [43]) to relatively steep (~30°) in the south (Figure 1; e.g., [44, 45]). Even though the present-day subduction regime has been active since at least Early Jurassic times ([46] and references therein), the flattening of the slab north of 33°S presumably began at ~19 Ma [47–49], finally achieving its subhorizontal configuration at ~7–6 Ma (for a review see [31, 43, 50]). It has been proposed that this flattening event is responsible for the absence of present-day magmatism between 27° and 33°S (Figure 1) [31, 50]. Several causal mechanisms have been suggested for triggering flat subduction at these latitudes, including (i) buoyancy of the slab due to the subduction of an aseismic ridge [50–52]; (ii) fast trenchward motion of the overriding plate

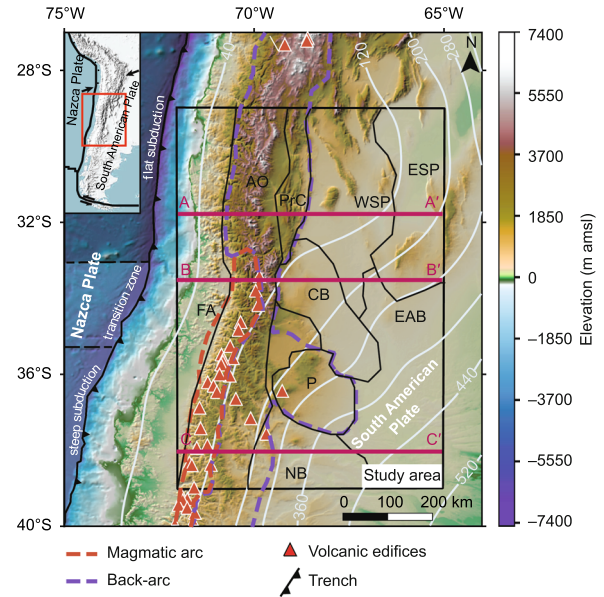


FIGURE 1: Topography and bathymetry of the region based on the ETOPO1 global relief model [60], showing the extent of the subduction segments with steepening subduction angles from north to south. The boundaries between the subduction segments are indicated with black dashed lines. The depth contours (km below sea level) of the top of the slab from SLAB2 [61] are shown in white lines. The black rectangle denotes the extent of the area modeled in this study. The boundaries between the main morphotectonic provinces are shown in black lines. Red triangles show the location of active volcanic edifices [62]. The purple dashed lines enclose the backarc domain and the red dashed lines the magmatic arc. The magenta lines show the locations of the cross sections in Figure 13. Abbreviations of main tectonic provinces: AO = Andean orogen, CB = Cuyo Basin, ESP = Eastern Sierras Pampeanas, EAB = extra-Andean basins, FA = forearc, NB = Neuquén Basin, P = Payenia volcanic province, Prc = Precordillera, WSP = Western Sierras Pampeanas.

that inhibits slab rollback and drives the trench to retreat [53]; (iii) stagnation of the oceanic plate in the mantle transition zone [54, 55]; and (iv) enhanced coupling between the oceanic and continental plates due to the greater strength of the continental plate [56–59].

In the SCA, surface heat flow, shallow subsurface temperatures, and magmatic activity vary significantly across the subduction system, which generally has been attributed to the geometry of the subducting Nazca plate [53, 63–71]. Earlier studies [63, 64, 68, 72], based on lower surface heat flow values (20–70 mWm^{-2} vs. 50–120 mWm^{-2}), suggested that the flat-slab segment is colder than its steeper counterparts, a hypothesis which was also supported by geodynamic numerical modeling [53, 65, 66] and seismic tomography [67, 69–71]. According to the latter studies, low v_p/v_s ratios (P wave/ S wave velocity < 1.75) characterize the flat-slab segment in the northern part of the SCA, in contrast to the higher v_p/v_s ratios encountered to the south, which are within the range typically found for most subduction zones [73]. The thermal contrast between the two differently dipping segments in the SCA is commonly linked to variations in the extent of the mantle wedge and arc magmatism, both

of which are drastically reduced in the flat-slab segment [31, 73–77]. All previous studies therefore seem to suggest that the forearc is an area with low surface heat flow in response to the subduction of cold oceanic crust at shallow depths.

These interpretations have recently been challenged by local-scale studies which indicate that parts of the thermal variations in the lithosphere of the SCA are not related to the effect of the subducting plate [25, 78–82]. For example, Sánchez et al. [80, 81] provided evidence for a significant difference in surface heat flow between the orogen (85–95 mWm^{-2}) and the foreland (~45–60 mWm^{-2}) at the latitudes of the flat-slab region and proposed structural and/or compositional variations within the crust and different heat flow input at the base of the lithosphere as possible reasons for this phenomenon. However, none of these hypotheses have yet been validated by a detailed study of the configuration of the lithosphere in terms of its geometry and composition.

In light of the open questions, we aim to test in this contribution how mantle thermal anomalies and first-order structural and lithological heterogeneities in the overriding plate across and along strike of the subduction system affect the thermal field of the SCA. In order to do so, we followed a data-based modeling approach. Seismic shear wave velocities [83] were converted to temperatures to obtain the deep thermal field in the mantle and across the subduction interface. In the model domains shallower than 50 km, where no mantle shear wave velocity data are available for conversion to temperatures, we calculated the steady-state conductive thermal field. To test the assumption of thermal equilibrium, we analyzed the effects of time-dependent processes related to subduction dynamics by carrying out a transient numerical analysis for the portion of the model domain with lack of constraints from the seismic tomography. Steady-state conductive temperatures in the shallow model domain were computed based on an existing 3D structural and density model of the SCA [58], which is consistent with available geological and geophysical data. We assigned thermal properties to the sedimentary cover rocks, the crystalline crust, continental lithospheric mantle, and oceanic plate according to the lithological characteristics of the units that previously have been derived from surface geology as well as from seismic velocities and modelled densities [58]. This allowed us to evaluate the control of the lithospheric structure on the resulting temperature distribution. The validity of the inferred thermal structure is assessed by comparison with temperature and surface heat flow measurements available for the studied area and a detailed sensitivity analysis of the model. One main challenge of this approach is related to the sparse coverage of thermal measurements in certain parts of the model. To address this problem, our results are qualitatively compared with other proxies of the thermal state of the area with larger spatial coverage, including seismic attenuation and elastic thickness patterns. As a result, we have obtained a 3D thermal model of the SCA and adjacent foreland regions that describes the relative temperature variations between the geological units of different composition and lateral and depth extents. Finally, this model allows us to make a qualitative analysis of the thermal feedback mechanisms between these different geological units.

1.1. Lithospheric Configuration of the Southern Central Andes. The main thickness and density variations of the layers constituting the SCA lithosphere were recently described in a 3D lithospheric-scale, density, and structural model of the SCA [58]. This model was constrained by an array of geological and geophysical data, including seismic reflection and refraction profiles, seismic tomography, sediment-isopach maps, and gravimetric observations ([61, 83–86]; see references in [58]). This structural geological model covers a region of 700 km by 1100 km with a horizontal resolution of 25 km and a depth of 200 km below mean sea level (bmsl), comprising the forearc, the Andean orogen, and the foreland regions. The vertical resolution varies as a function of the thickness of the corresponding layers, which were mainly defined on the basis of density contrasts. These layers comprise from top to bottom: (1) water; (2) marine sediments; (3) continental sediments; (4) upper continental crystalline crust; (5) lower continental crystalline crust; (6) continental lithospheric mantle; (7) shallow oceanic crust; (8) deep oceanic crust; (9) oceanic lithospheric mantle; and (10) oceanic sublithospheric mantle. Figure 2 illustrates the main structural features of the 3D model (see Rodríguez Picada et al. [58] for more details).

Overall, maximum sedimentary thicknesses occur in the Cuyo and Neuquén basins (Figure 2(a)). The Andean orogen has a thicker crystalline crust (55 km) than the forearc (~35 km) and the foreland (~30 km) (Figure 2(b)). The remaining parts of the backarc and the foreland can be subdivided into three crustal domains: (i) a thick northern domain (40–60 km); (ii) a thin southern domain (~20 km); and (iii) a central domain with intermediate crustal thickness (35–45 km). The areas with the greatest upper crustal thickness comprise the orogen (20–40 km) and the Payenia volcanic province (20 km). In contrast, in the Neuquén Basin the upper crustal thickness thins out to 5 km (Figure 2(c)). The greatest lower crustal thickness (~30–45 km) exists in the northern part of the backarc and foreland regions of the Precordillera and Sierras Pampeanas (Figure 2(d)).

2. Modeling Approach

The general workflow followed in this study is illustrated in Figure 3(a). Figure 3(b) shows the 3D model box, where different thermal modeling approaches and corresponding thermal boundary conditions were applied. To predict the present-day thermal configuration of the SCA and discuss its controlling factors, we subdivided the model volume into two domains: a deep domain between a depth of 50 and 200 km bmsl, where temperatures were converted from S wave seismic velocities (here referred to as “ v_s -to- T conversion”), and a shallow domain, including the crust and uppermost mantle down to a depth of ~50 km bmsl, where the steady-state conductive thermal field was calculated using as input the 3D structural and density model of the area [58]. The reasons for this subdivision are as follows: the v_s -to- T conversion being developed for application to mantle rocks and the limited quality of mantle velocity data for depths shallower than 50 km [83].

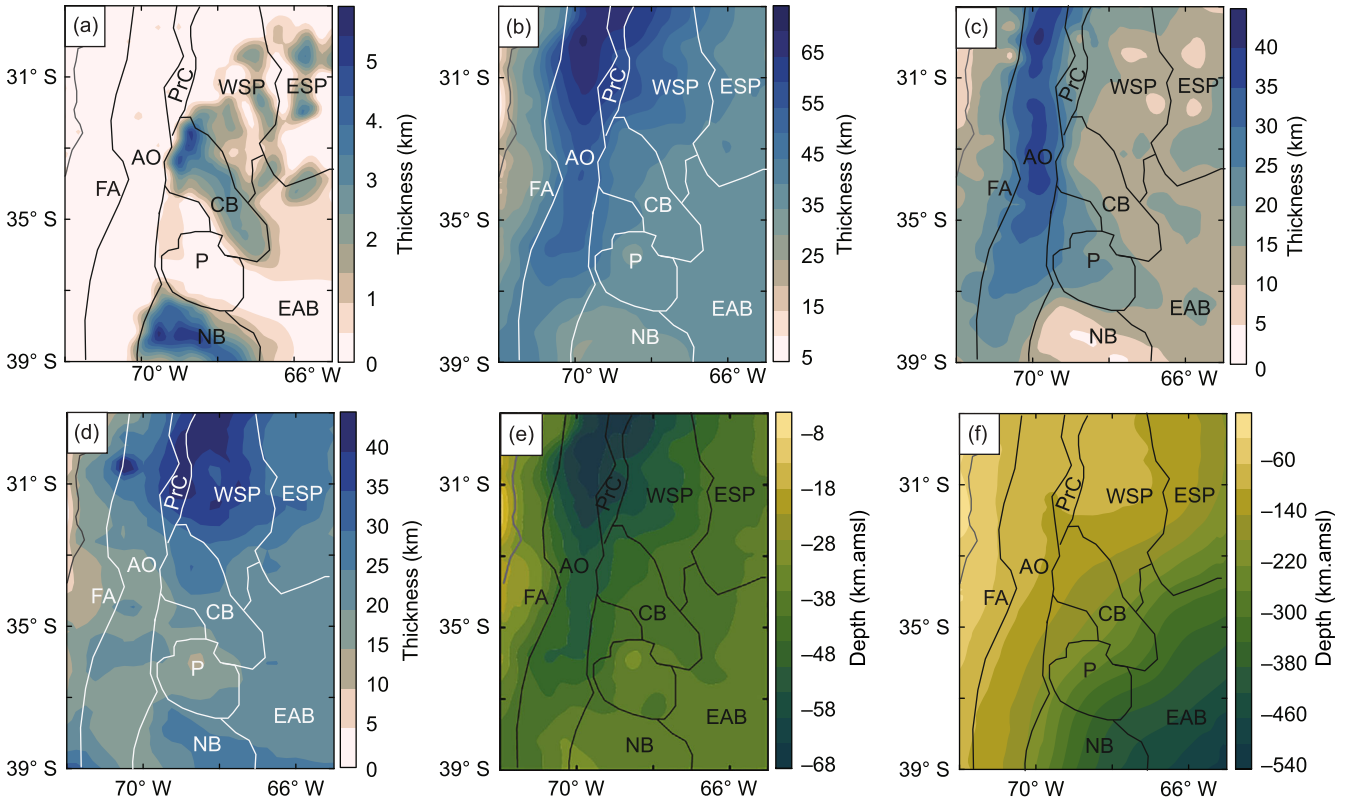


FIGURE 2: Main structural features of the studied lithosphere from the 3D structural geological model of [58]: thickness of (a) marine and continental sediments; (b) continental crystalline crust; (c) felsic upper continental crystalline crust; (d) mafic lower continental crystalline crust; (e) depth to the continental Moho; and (f) depth to the subduction interface, coinciding with the top to the oceanic crystalline crust west of the trench and with the top surface of the slab east of the trench.

2.1. Calculation of Temperatures in the Deep Domain. To estimate mantle temperatures between 50 km and 200 km, we used the results of the *S* wave mantle tomography of Assumpção et al. [83]. This tomographic model is an updated version of the *S* wave tomography of Feng et al. [91] for the South American region, where the velocity structure of the upper mantle was constrained through the joint inversion of *S* and Rayleigh waveforms and fundamental mode group velocities of Rayleigh waves. The original data set is restricted to depths between 50 km and 400 km, with a horizontal resolution of approximately 25 km [91]. Our choice on the tomography of Assumpção et al. [83] rather than other global tomographic models covering the study area [92] stems from the fact that this model has a more refined lateral and vertical resolution and offers a better spatial correlation between high-velocity features and the track of the slab ([61]; Figure S1 in supporting information).

To compute temperatures from *S* wave velocities, we used the python tool VelocityConversion [88] which is a modified version of the original approach by Goes et al. [87]. The method by Goes et al. [87] is based on laboratory measurements of mantle mineral properties and considers anharmonicity and anelasticity of seismic waves. The equation that relates v_s in a rock with a given composition *X*

under a temperature *T* and a pressure *P* condition is written as follows:

$$v_s(P, T, X, \omega) = \sqrt{\frac{\mu(P, T, X)}{\rho(P, T, X)}} - (1 - \varepsilon(\omega, T, a)), \quad (1)$$

where ω is the wave frequency, μ is the shear modulus, ρ is the density, *a* is the frequency exponent, and ε is the attenuation term. ε is defined as

$$\varepsilon(\omega, T, a) = \frac{2}{Q(\omega, T) \cdot \tan(\pi a/2)}, \quad (2)$$

with *Q* being the attenuation due to anelasticity, described as

$$Q(\omega, T) = A \cdot \omega^a \cdot \exp\left[\frac{a(H + P \cdot V)}{RT}\right], \quad (3)$$

where *A* and *R* are the anelastic and universal gas constants, respectively; *H* is the activation energy; and *V* is the activation volume.

From Equation (1), it is clear that the computation of mantle temperatures requires to define the mantle composition *X* described in terms of its main mineral phases (olivine,

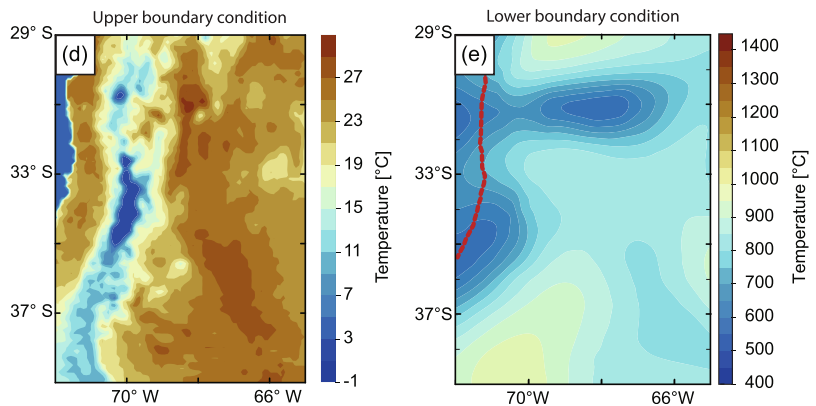
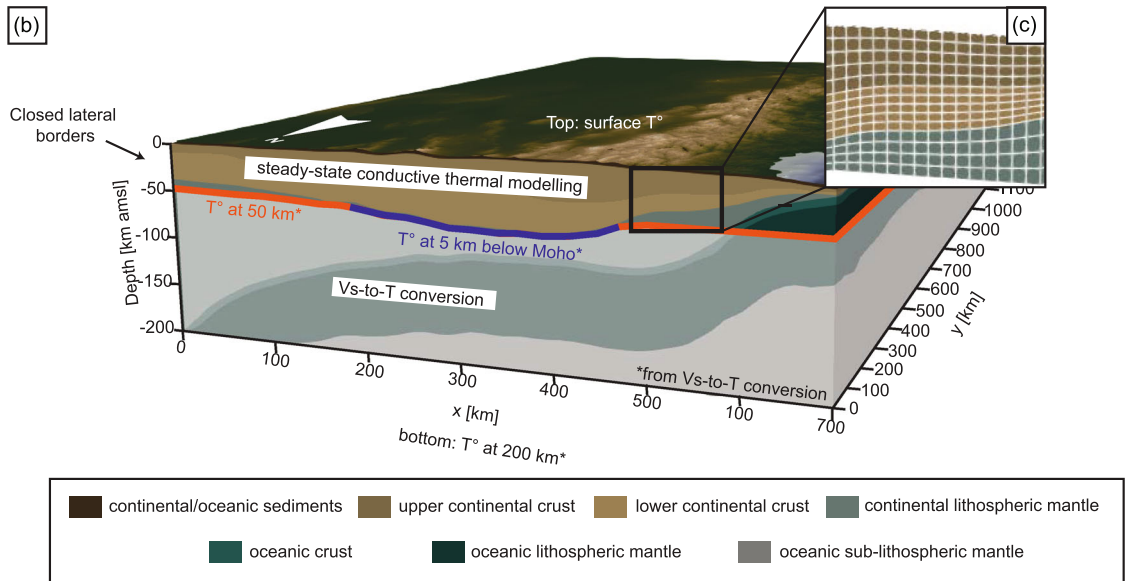
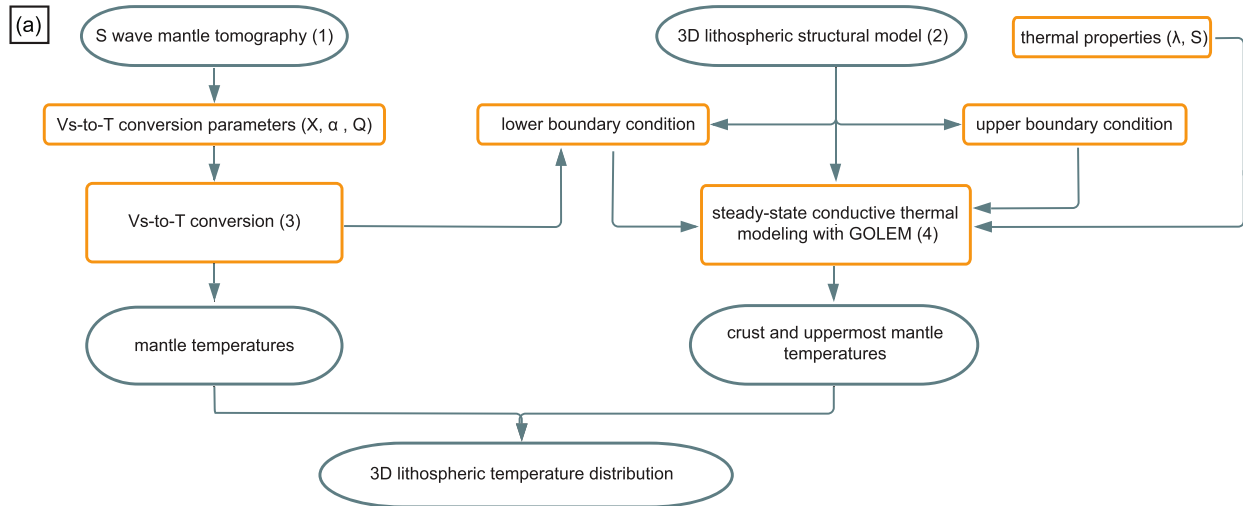


FIGURE 3: (a) General workflow followed in this study to estimate temperatures in the SCA lithosphere. (b) 3D model box indicating the lithospheric domains where the conversion of seismic velocities (grey-shaded area) and the steady-state conductive modeling (non grey-shaded area), respectively, were applied. The types of thermal boundary conditions considered for the conductive steady-state modeling are also shown. (c) Close-up of finite element mesh used for the steady-state conductive thermal modeling. (d) Upper and (e) lower boundary conditions applied to the conductive steady-state model. (1) Rodriguez Piceda et al. [58]; (2) Assumpção et al. [83]; (3) Goes et al. [87]; Meeßen [88]; (4) Cacace and Jacquey [89]; Jacquey and Cacace [90]. λ = thermal conductivity, S = radiogenic heat production; X = mantle composition, α = thermal expansion coefficient, Q = anelasticity.

orthopyroxene, clinopyroxene, and spinel/garnet) and iron content [87]. For each mineral phase, temperature, and pressure (up to 6 GPa), the density ρ and the elastic modulus M (shear modulus μ and/or compressibility k) from their values at the reference state (P_0, T_0) are calculated as

$$\rho(P, T) = \rho(P_0, T_0) \cdot \left[1 - \alpha(T - T_0) + \frac{P - P_0}{k} \right] \quad (4)$$

$$M(P, T) = M(P_0, T_0) + (T - T_0) \cdot \frac{\partial M}{\partial T} + (P - P_0) \cdot \frac{\partial M}{\partial P} \quad (5)$$

where α is the thermal expansion coefficient.

The implementation by Meeßen [88] calculates the v_s and the corresponding density at each depth in the seismic tomography for temperatures between 300 and 3000 K in steps of 1 K. For the density computation, lithostatic pressure is computed relying on the AK135 seismic model [93]. At each grid point, the algorithm compares the computed v_s with those from the tomographic model, by performing a look-up method over the table and choosing the two closest values to the velocity from the tomography. Then, the temperatures and corresponding densities are linearly interpolated to obtain the final values.

For this study, we chose different mantle compositions (spinel or garnet), listed in Table 1, according to the respective stable aluminum phase at depth [94]. For shallow depths (50–80 km), a mantle composition corresponding to a spinel lherzolite was assigned, in accordance with mantle xenoliths found in the Payenia volcanic province [95, 96]. Between 80 km and 200 km, the stable composition was assumed to correspond to garnet lherzolite [97]. Mineral properties α , $\rho(P_0, T_0)$, $M(P_0, T_0)$, $\partial M/\partial T$, and $\partial M/\partial P$ were taken from Cammarano et al. [98] and Goes et al. [87]. The thermal expansion coefficient α was assumed constant for each mineral phase. The frequency exponent a and anelasticity parameters A , H , and V were taken from Sobolev et al. [99] (Table 2).

The temperature configuration derived from the v_s -to- T conversion in the parameter space of v_s and depth is shown in Figure 4, which also depicts three 1-D v_s profiles representative of the orogen at the latitudes of the flat slab, the steep slab, and the transition zone. In general, temperature increases with increasing depth and decreasing velocity. The largest temperature variations occur for depths shallower than 100 km and high v_s ($>4.6 \text{ km s}^{-1}$), which is characteristic of the flat-slab domain.

2.1.1. Sensitivity of the v_s -to- T Conversion. Quantifying uncertainties in the v_s -to- T conversion is difficult due to the combined effects of uncertainties related to the conversion parameters (i.e., anelasticity model and mantle composition, [100]). An additional source of uncertainty is the S wave tomography, as a 0.1% perturbation in v_s , for example, can translate into temperature variations of 50° – 250°C . Previous studies [87, 100] assumed a temperature uncertainty of 150°C in the v_s -to- T conversion at Moho depths, but recognized larger uncertainties at greater depths. We therefore

TABLE 1: Mantle composition used for the conversion of v_s to temperatures [87, 88].

Mantle unit	Lithology	Ol	Opx	Cpx	Sp	Gnt	Xfe
50-80 km	Spinel lherzolite ^{1,2}	0.60	0.17	0.19	0.04	—	0.10
80-200 km	Garnet lherzolite ³	0.63	0.30	0.02	—	0.05	0.08

Note. Ol = olivine; Opx = orthopyroxene; Cpx = clinopyroxene; Sp = spinel; Gnt = garnet. The sum of mineral fractions is equal to 1. Xfe = iron content in molar fraction. Xfe is calculated as $(1 - Mg\#)/100$, where $Mg\#$ is the magnesium number. ¹Conceição et al. [95]; ²Jalowitzki et al. [96]; ³Maaløe and Aoki [97].

TABLE 2: Anelasticity parameters used for the conversion of v_s to temperatures [99].

Anelastic constant, A	0.48
Activation energy, H [J mol^{-1}]	$5 \cdot 10^5$
Activation volume, V [$\text{m}^3 \text{mol}^{-1}$]	$2 \cdot 10^{-5}$
Frequency exponent, a	0.15

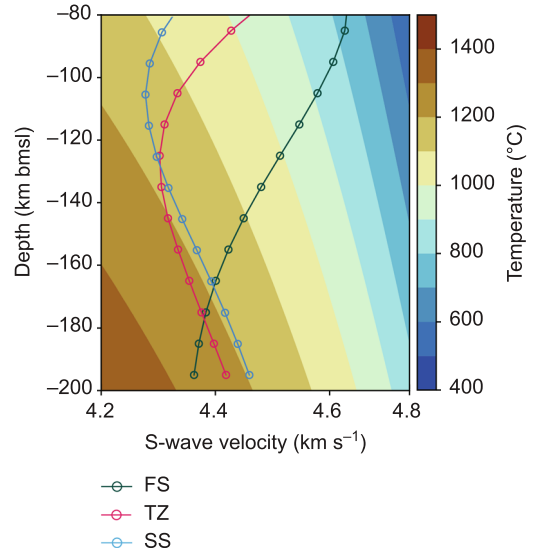


FIGURE 4: Mantle-temperature distribution as a function of v_s and depth (obtained using VelocityConversion; [88]) overlain by 1-D v_s profiles of the seismic tomography of [83]. FS = flat-slab domain; TZ = transition domain; SS = steep-slab domain.

reexamined the uncertainty of the conversion method of Goes et al. [87] by testing the model sensitivity with respect to mantle composition X , thermal expansion coefficient α , and attenuation Q . Regarding the conversion method, although several approaches exist [101–104], we only tested the method of Priestley and Mckenzie [102] as implemented by Meeßen [105] (Model PM). In a first step, we set up a model (“reference model” hereafter) based on the following parametrization: (i) mantle composition X corresponding to a garnet lherzolite (Table 1); (ii) constant expansion coefficient α ; and (iii) anelasticity Q by Sobolev et al. [99] (Table 2). In a second stage, we tested alternative models by varying one parameter at a time: (i) mantle composition

TABLE 3: Lithology and thermal properties assigned to the units of the 3D structural model [58].

Layers	λ [$\text{Wm}^{-1}\text{K}^{-1}$]	S [μWm^{-3}]	Lithology
Continental/oceanic sediments	2.00 ¹	1.00 ²	Siliciclastic
Upper continental crystalline crust	3.40 ¹	2.00 ²	Dioritoid
Lower continental crystalline crust	2.50 ¹	0.40 ³	Mafic granulite
Oceanic plate	Shallow crust	1.80 ¹	Basalt
	Deep crust	2.87 ⁵	Eclogite
Continental and oceanic lithospheric mantle	2.24 ⁴	0.01 ²	Moderately depleted lherzolite

Note. λ = bulk thermal conductivity; S = radiogenic heat production. ¹Čermák and Rybach [118]; ²Viřilá et al. [121]; ³Hasterok and Chapman [119]; ⁴Xu et al. [122]; ⁵He et al. [120].

(spinel model), (ii) thermal expansion coefficient (α model), and (iii) attenuation (Q2 Model). In all cases, the conversion was limited to the depth interval of 50–200 km, as thought to be representative of the lithospheric mantle. A detailed description of the setup of these alternative models is provided in the Supporting information (Text S1). In Section 3.1, we discuss in greater details the results from the same sensitivity analysis as applied to the tomography of Assumpção et al. [83], while in Section 4.1.2, we open a discussion on the implications of this sensitivity analysis on the modeled deep thermal field.

2.2. Calculation of Temperatures in the Shallow Domain. To estimate temperatures in the shallow domain (that is in the crust and the mantle above 50 km), we used the geometry of the lithospheric layers of the 3D model as described in Section 1.1 [58] as input to solve for the steady-state heat conduction equation (Figure 2). Under steady-state conditions, this equation reads as follows:

$$\text{div}(\lambda \nabla T) = -S, \quad (6)$$

where T is the temperature (K), λ is the bulk thermal conductivity ($\text{Wm}^{-1}\text{K}^{-1}$), and S is the radiogenic heat production (Wm^{-3}). Equation (6) describes the conservation of internal energy under the assumption of thermal equilibrium. This last assumption might be over-restrictive especially for young slabs, where the additional effects from thermal advection from the advancing megathrust might be relevant. We discuss the influence of deviations from thermal equilibrium due to advection of the cold subducting plate in Section 4.1.1.

Temperatures were calculated with the finite element code GOLEM [89, 90]. For the thermal computation, three modifications were made to the original 3D configuration of Rodríguez Piceda et al. [58]. First, the water layer was removed, thus treating the topography/bathymetry as the top of the model (cf. Figure 1). Second, the horizontal resolution was increased from 25 km in the original structural model to 5 km, and, third, the layers were vertically refined by a factor of 3 to 32 in order to ensure that (i) each layer has at least three finite elements and (ii) most of the model domain is represented by a cubic finite element to ensure faster numerical convergence (Figure 3(c)). These modifications ensured to properly solve the temperatures in each

node of the mesh without significantly increasing computational time.

Each unit of the 3D lithospheric model was populated with constant thermal properties (Figure 3(a); bulk conductivity λ and radiogenic heat production S) according to its main lithology (Text S2 in supporting information). The characteristic lithologies, in turn, were selected based on the comparison between gravity-constrained densities [58] and mean P wave velocities [67, 106–109], combined with rock-property compilations [110, 111] and other seismic properties [70, 112–117]. A range of thermal properties [118–122] related to the chosen lithology for each layer was additionally tested until the best fit was achieved with a compilation of borehole temperatures mainly limited to the foreland basins [79]. Table 3 summarizes the chosen values for each layer of the final (best fitting) model. A sensitivity analysis of the model results to the tested range of the thermal properties indicate that the modeled temperatures are most sensitive to variations in the thermal conductivity of the upper continental crystalline crust and the mantle (Text S3 in supporting information).

To close Equation (6), Dirichlet boundary conditions (i.e., fixed temperatures) were assigned along the top and base of the model. The upper thermal boundary condition was set at the topography/bathymetry (Figure 3(b)), with temperatures extracted from the ERA-5 land database ([123]; Figure 3(d), Text S4 in supporting information). The lower boundary condition was set at the depth of the upper bound of the v_s -to- T conversion: a constant depth of 50 km bmsl for areas where the Moho is shallower than 50 km bmsl and at a surface 5 km deeper than the Moho where this interface is deeper than the abovementioned threshold (Figure 3(b)). The reason for choosing this depth for the boundary condition stems from the fact that at shallower depths, the seismic velocity from the tomography of Assumpção et al. [83] reflects both mantle and crustal components. The temperature distribution at this boundary was derived from the v_s -to- T conversion (Figure 3(e); [83]; Section 2.2).

3. Results

3.1. Thermal Field of the Deep Domain. From the conversion of S wave velocities taken from the tomography of Assumpção et al. [83], we obtained the lower boundary

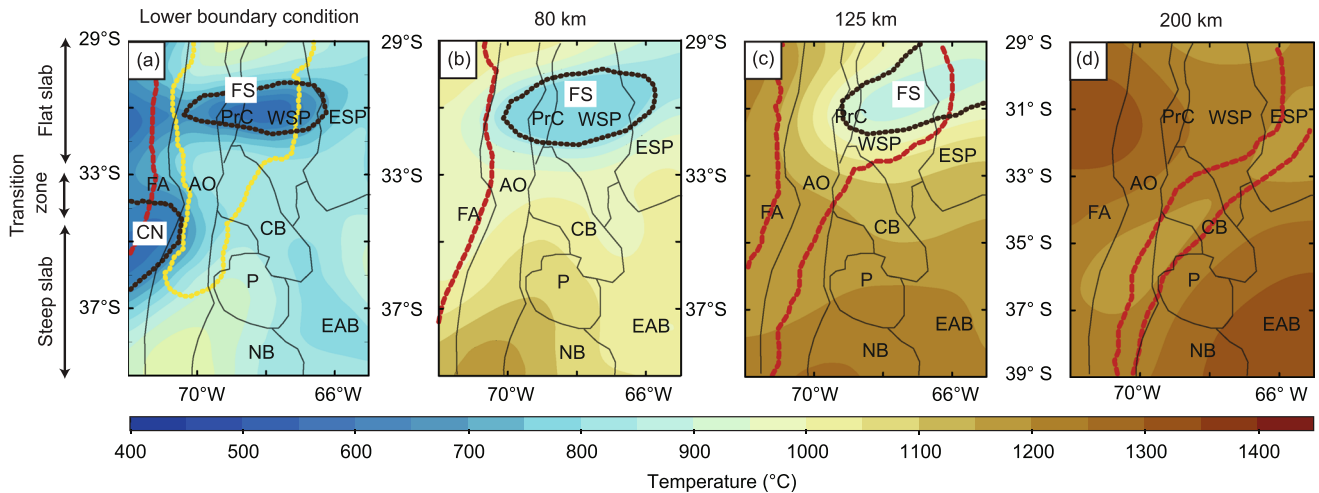


FIGURE 5: Temperature distribution obtained from the v_s -to- T conversion using the tomography of Assumpção et al. [83] at depths of the following: (a) 50 km bmsl and at 5 km below the Moho in the interior of the area limited by the yellow line (lower boundary condition of the steady-state model); (b) 80 km bmsl; (c) 125 km bmsl; and (d) 200 km bmsl; black lines in (a)–(c) indicate the extent of the cold mantle areas: CN = cold nose, FS = flat slab. Red lines denote the intersections of the depth levels with the top and the bottom of the slab, respectively [61].

condition of the steady-state conductive model (Figure 5(a)) and the mantle-temperature distribution for the ~50–200 km depth interval (Figures 5(b)–5(d)). Across the lower boundary condition, temperatures roughly range between 600 °C and 1000 °C. Two domains with temperatures of <700 °C are identified: (i) a cold nose (CN) between 70°W and 72°W, beneath the forearc in the central and northern portion of the study area, and (ii) a domain farther to the east where the slab flattens (FS) between 29.5°S and 32.5°S. The CN extends eastward above the transition zone and the steep-slab segment and is significantly attenuated above the flat-slab segment (Figure 5(a)). With increasing depth (>75 km bmsl), this thermal feature is no longer visible, while the cold FS domain extends vertically over the entire mantle column of the overriding plate (Figures 5(a)–5(c)). At 80 km bmsl, temperature increases to the SW, with maximum values (~1100 °C) located between 37° and 39°S and 70° and 72°W (Figure 5(b)). At 125 km bmsl, the temperatures follow a similar pattern as at 80 km depth, but differ in absolute value, with the cold FS domain reaching temperatures between 850 °C and 900 °C (Figure 5(c)). Towards the marine domain and to the south of the study area, temperatures increase up to 1300 °C. At the base of the model (200 km bmsl), temperature ranges between ~1200 °C and ~1350 °C, with the lowest temperatures correlating spatially with the track of the slab ([61]; Figure 5(d)).

We evaluated the effect of uncertainties in the parametrization of the v_s -to- T conversion applied to the seismic tomography of Assumpção et al. [83] by comparing the model described above with alternative model scenarios (for details, see Text S1 in Supporting Information). Figure 6 shows these alternative models in terms of the residual temperature at the lower thermal boundary condition of the steady-state model and at depths of 80, 125, and 200 km. The S wave velocity distributions [83] at those depths are also depicted.

The change from a garnet-and-spinel model (reference model; Table 1) to a mantle composed only of the spinel variant exerts the strongest effect on the resulting temperature at shallow depths and particularly where v_s is >4.5–4.6 km s⁻¹. The greatest temperature difference between the reference and the spinel models is 200 °C (Figures 6(e) and 6(f)). In our study region, v_s of such high magnitudes characterizes the forearc and the flat-slab segment in the northern part of the foreland (Figure 6(a)). The temperature residuals decrease with increasing depth, where lateral variations of v_s are less distinct (Figures 6(g) and 6(h)).

The conversion method of Priestley and McKenzie [102] yields the largest temperature differences among all the alternative models tested, predicting up to ±400 °C difference for areas with high (>4.5 km s⁻¹) and low (<4.5 km s⁻¹) v_s , respectively (Figures 6(q) and 6(r)), as compared to the reference model converted based on Goes et al. [87].

3.2. Thermal Field of the Shallow Domain. From the steady-state conductive approach, we computed the thermal field of the crust and uppermost mantle to the depth of the lower boundary condition (Figures 7 and 8) and the surface heat flow (Text S5 in Supporting Information; Figures 8 and 9). Figure 7 shows the temperature distribution at depths of 2, 5, 10, 20, 25, 30, 35, 40, and 45 km bmsl and at the Moho. In Figure 8, we plot the modeled thermal field and the configuration of the main lithospheric units together with variations in predicted surface heat flow compared to available observations [63, 68, 126], along three representative E-W cross sections of the flat slab, the transition zone, and the steep-slab subduction segments.

At 2 km bmsl, the temperatures range between 15 °C and 165 °C (Figure 7(a)). As expected, the warmest areas are those with the highest topography (4–6 km height; cf. Figure 1) and the largest upper crustal thickness (30–40 km, cf. Figure 2(c)), which correspond to the central

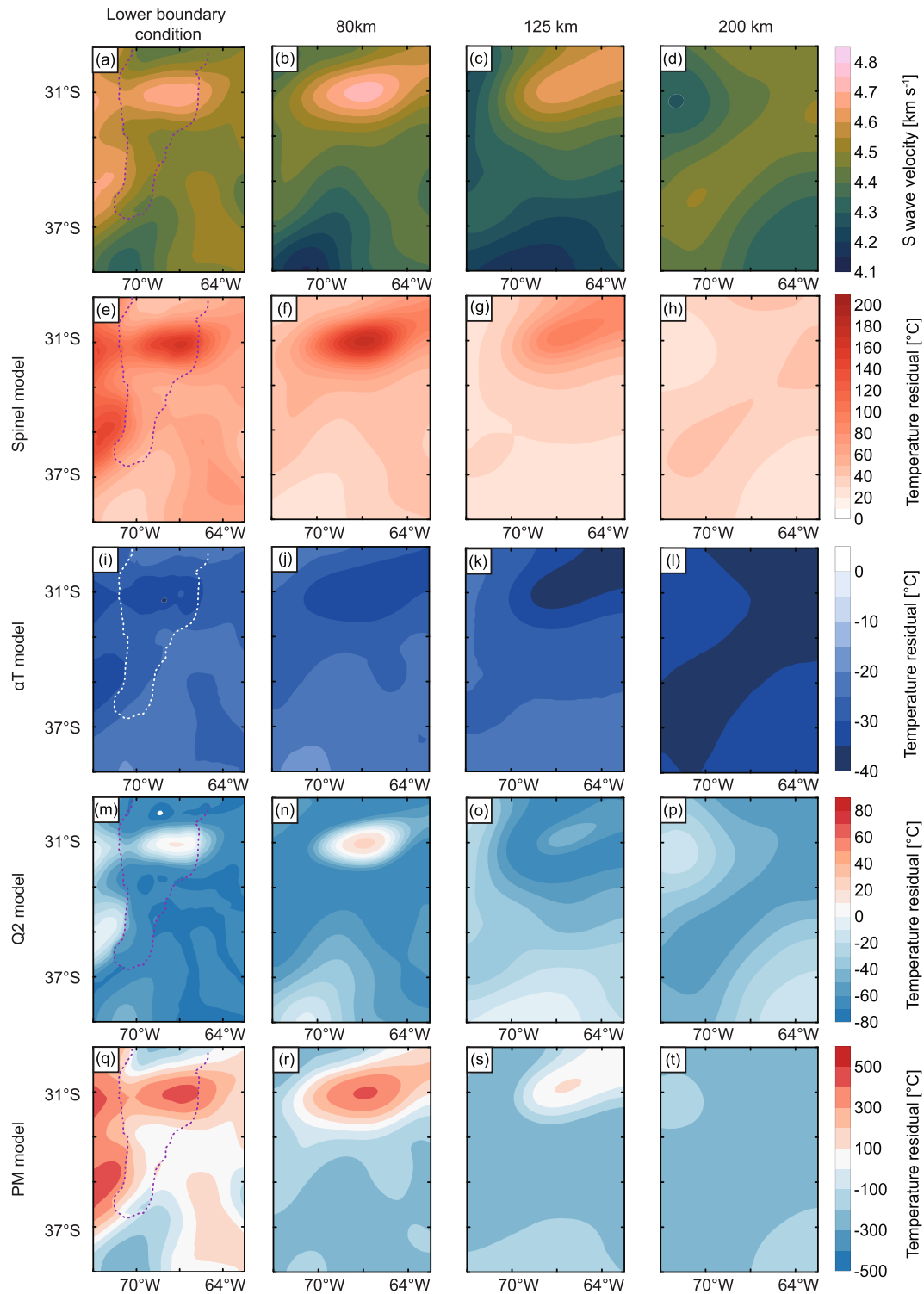


FIGURE 6: Results from sensitivity analysis of the v_s -to- T conversion (text S1 in supporting information). Slices at depths of the lower boundary condition of the steady-state model, 80, 125, and 200 km bmsl showing the distribution of the following: (a–d) S wave velocity from the seismic tomography of Assumpção et al. [83]; (e–t) temperature residual (difference between the temperature fields of the reference model and each alternative configuration); (e–h) spinel model, with a mantle composition of spinel lherzolite [95, 96] throughout the whole depth range; (i–l) αT model, with temperature-dependent thermal expansion coefficient [87, 98, 124]; (m–p) Q2 model, with anelasticity parameters from Berckhemer et al. [125]; and (q–t) PM model, with v_s -to- T conversion following Priestley and Mckenzie [102]. The dotted lines in (a), (e), (i), (m), and (q) mark the intersection with the 45 km depth contour of the Moho.

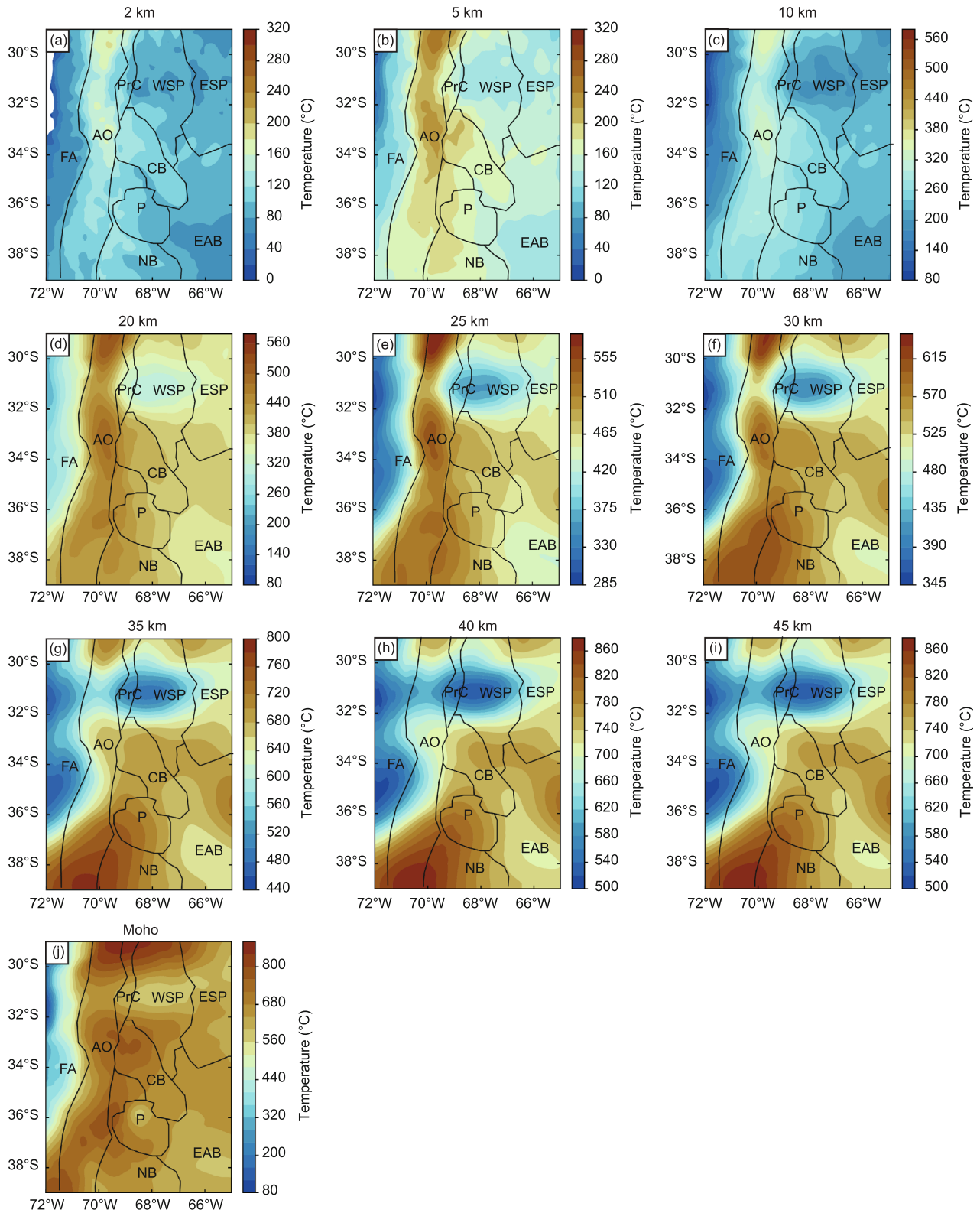


FIGURE 7: Modeled temperature distribution at different depths below mean sea level: (a) 2 km, (b) 5 km, (c) 10 km, (d) 20 km, (e) 25 km, (f) 30 km, (g) 35 km, (h) 40 km, (i) 45 km, and (j) Moho. Boundaries of the main morphotectonic provinces are also marked with black lines; for abbreviations, see Figure 1.

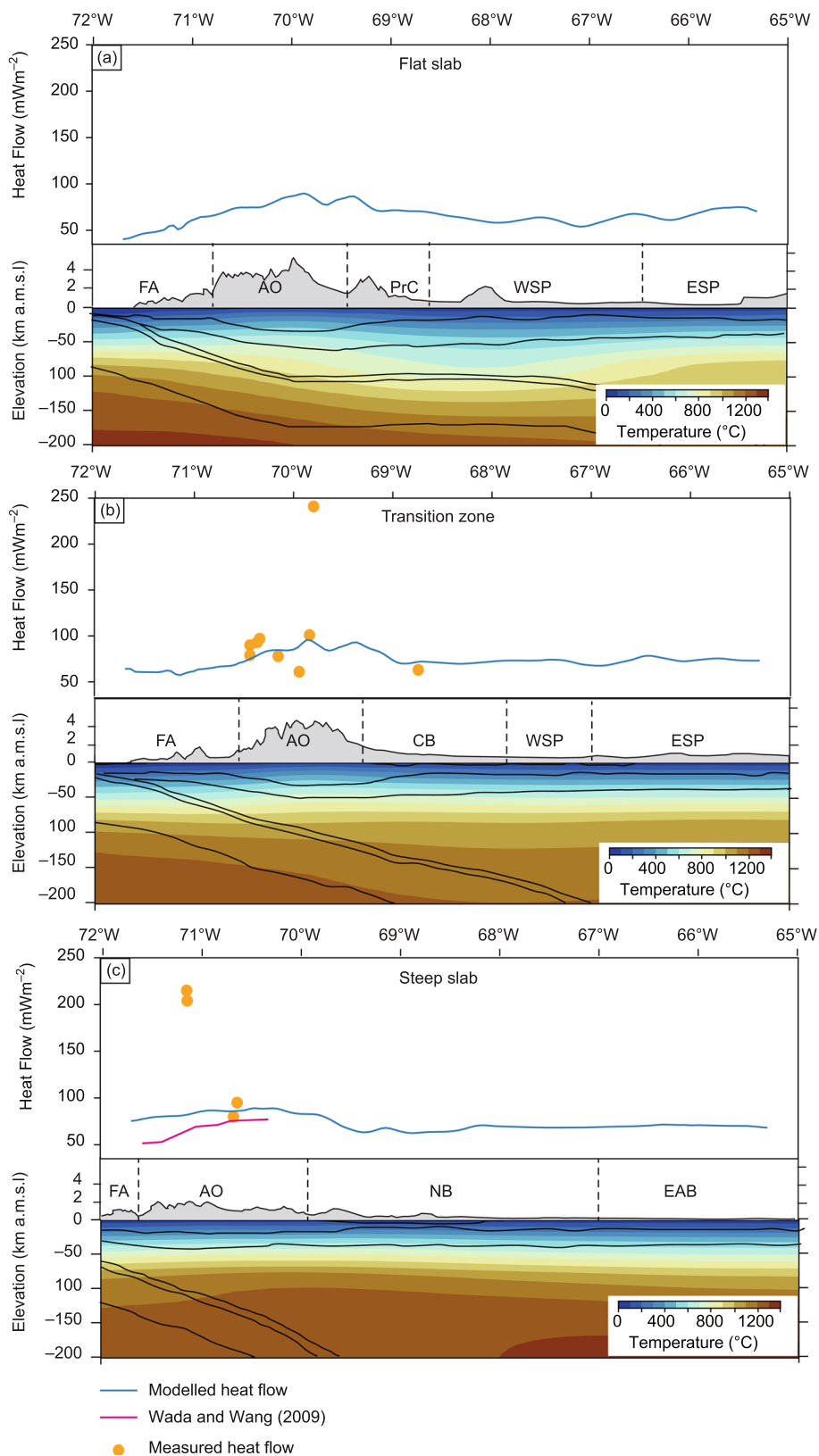


FIGURE 8: E-W cross sections showing modeled and measured surface heat flow (upper panels) and temperature distribution (lower panels) representative of the subduction segments of (a) flat slab, (b) transition zone, and (c) steep slab. Heat flow measurements are derived from Hamza and Muñoz [63] and Uyeda and Watanabe [68]. In (c), a modelled heat flow according to Wada and Wang [127] is also overlain. For location of the profiles and abbreviations of the main morphotectonic provinces, see Figure 1.

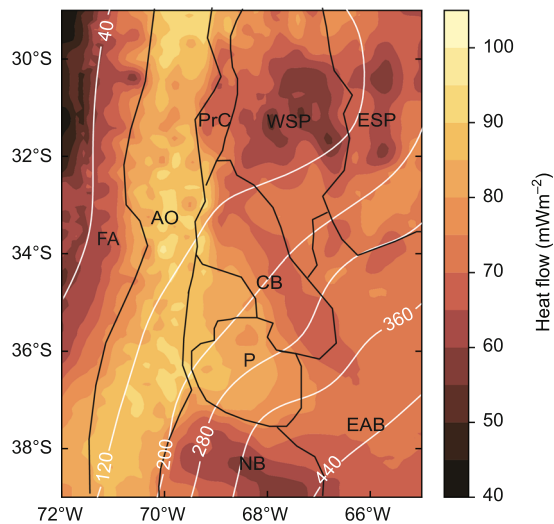


FIGURE 9: Modeled surface heat flow. Depth contours (km) of the top of the oceanic crust from SLAB2 [61] are shown in white lines. Boundaries of the main morphotectonic provinces are also marked with black lines; for abbreviations see Figure 1.

and northern segments of the Andean orogen. In addition, the forearc is characterized by an overall lower temperature than the orogen (40–80 °C), but by a more pronounced lateral gradient with values increasing toward the Andes. The foreland and low-elevation backarc regions are characterized by a wide temperature range (60–115 °C), with warmer temperatures in the Precordillera, the Payenia volcanic province, and the Cuyo and Neuquén basins. Down to 25 km bmsl, the spatial trends of temperature distribution are similar to those observed at shallow depths, but with different absolute values (Figures 7(b)–7(e)).

The thermal contrast between the warm orogen and the relatively cold forearc, backarc, and foreland regions is more pronounced with increasing depth (e.g., differences of ~110 °C at 10 km bmsl and ~200 °C at 20 km bmsl; Figures 7(c) to 7(d) and 8). From 20 km bmsl downward, the temperature distribution partially resembles that of the lower boundary condition (Figure 5(a)). Lowest temperatures at these depths correlate spatially with the areas where the mantle is the coldest (CN and FS areas, Figure 5(a)). Here, the temperature minimum also correlates with a thick continental crystalline crust (~40 km, cf. Figure 2(b)) and thickened lower crust (>30 km, cf. Figure 2(d)).

The modelled surface heat flow varies laterally from minima of ~45–70 mWm⁻² in the oceanic domain, most of the forearc, and foreland to maxima across the orogen (80–100 mWm⁻²; Figures 8 and 9). We observe a remarkable spatial correlation between the surface heat flow distribution and continental crustal features: whereas high heat flow corresponds to areas with thick upper continental crystalline crust (>25 km; e.g., within the orogen and the Payenia volcanic province; cf. Figure 2(c)), low heat flow characterizes the deep sedimentary basins (~>3 km; e.g., the Neuquén Basin; cf. Figure 2(a)) and/or thick lower continental crystalline crust (>25 km; e.g., most of the Sierras Pampeanas; cf. Figure 2(d)).

3.3. Model Validation. As a first step in the validation process, we compared modeled temperature values with the published borehole measurements of Collo et al. [79], located mainly in the central and northern foreland (Figure 10(a)). The residual temperature (i.e., the difference between modeled and measured values) is shown in Figure 10(b). Figure 10(c) illustrates measured and modeled temperatures against depth, and Figure 10(d) shows the residual temperature against depth. In general, we obtain a good fit of approximately ± 20 °C between the borehole data and the modeled temperatures, with the exception of few outliers (Figure 10(c)). In the Cuyo Basin (33°S–69°W), positive temperature residuals tend to occur at shallow depths (<2 km), while negative residuals are detected at greater depths (Figure 10(b)). One plausible explanation for this trend is that the thermal conductivity of the Cuyo Basin sediments is slightly underestimated in our model. A larger thermal conductivity would translate in colder temperatures close to the basement surface and warmer temperatures close to the surface topography (see also sensitivity analysis in Text S3 of the supporting information).

Albeit limited in coverage, in a second step, we used available compilations of surface heat flow values within the SCA [63, 68, 126] to validate our thermal model. These measurements are not representative for the entire model domain as they are located mainly along the orogenic axis. They show a large variation in the magnitudes of the measured heat flow values (up to 250 mWm⁻²), even between spatially close measurements (Figure 10(c)). Figure 10(d) depicts the residual surface heat flow, i.e., the difference between the predicted and the measured surface heat flow, at the location of the measurements. Figure 10(e) is a histogram of residuals of surface heat flow. In general, the model underestimates the surface heat flow along the orogenic chain with respect to the measured values, with only ~25% of the predictions matching the observations (Figure 10(e)). The model does not reproduce the extremely high heat flow values (>150 mWm⁻²) reported for some volcanic areas in the axial sectors of the orogen. Additionally, due to its resolution, the model is not able to reproduce the observed variations in heat flow magnitudes between spatially adjacent measurements, which likely correlate to local features not resolved in our regional study (Figure 10(d)).

4. Discussion

4.1. Model Robustness and Sensitivity Analysis

4.1.1. Steady-State Assumption in the Shallow Lithosphere Domain. One main assumption in the calculation of the shallow temperature field was to consider that the lithosphere is in steady state. However, thermal equilibrium in the overriding plate can be disturbed by the advection of the cold subducting plate (e.g., [128, 129]). For instance, 2D kinematic models that consider this effect for the SCA [130] predict up to 200 °C colder temperatures at the subduction interface with respect to our model results (Figure S7 in Supporting Information). In light of these differences, a more appropriate modeling strategy would be

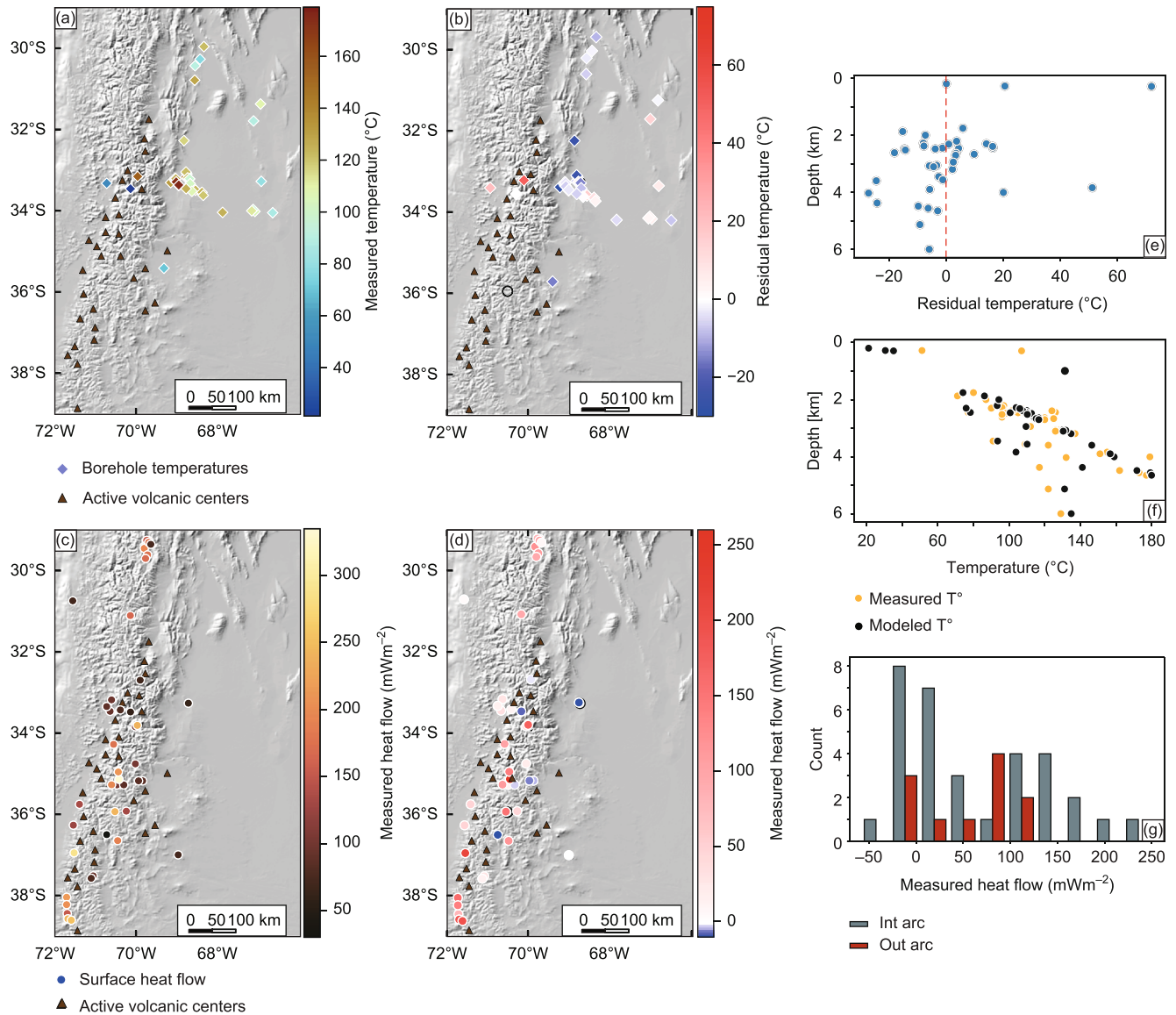


FIGURE 10: Shaded-relief image of the study area with superposed location of (a) borehole temperatures (diamonds, [79]), (b) residual temperature, (c) observed surface heat flow (circles, [63, 68]); and (d) residual surface heat flow. Residual values are obtained from the subtraction between observed and modeled values. Triangles in (a)–(d) show the locations of active volcanic centers [62]. (c) Comparison between measured (orange) and modeled (black) temperatures vs. depth. (d) Residual temperature vs. depth. (e) Histogram of residual heat flow, discriminating surface heat flow measurements within and outside the active volcanic arc (“int arc” and “out arc,” respectively).

to additionally account for this process. The caveat here is that performing such an analysis requires a detailed knowledge of the past temperature distribution in order to properly initialize the system. Unfortunately, we lack such constraints in the SCA. Given these considerations, we relied in our study on the assumption of steady-state conduction, where the results are less affected by the choice of the initial temperature condition, but are mainly determined by the model parameterization in terms of distribution of thermal properties and imposed boundary conditions (based on available observables in our study). Nonetheless, in an attempt to quantify the validity of this approximation for the SCA, we also computed a simulation that accounts for the

additional effects of advection of cold temperatures due to the motion of the subducting slab on the present-day thermal field of the shallow domain. To that end, we first computed the resulting thermal field from the advection of a cold thermal front along the subduction interface (i.e., top of the oceanic crust). In a following step, we imposed this thermal evolution as the lower boundary condition on the 3D configuration of the overriding plate and ran a transient simulation with a duration of 7 Ma, which represents the past period during which the subduction geometry remained unchanged [26, 43]. A detailed description of this analysis is provided in the supporting information (Text S6). The comparison between the initial and final time steps at

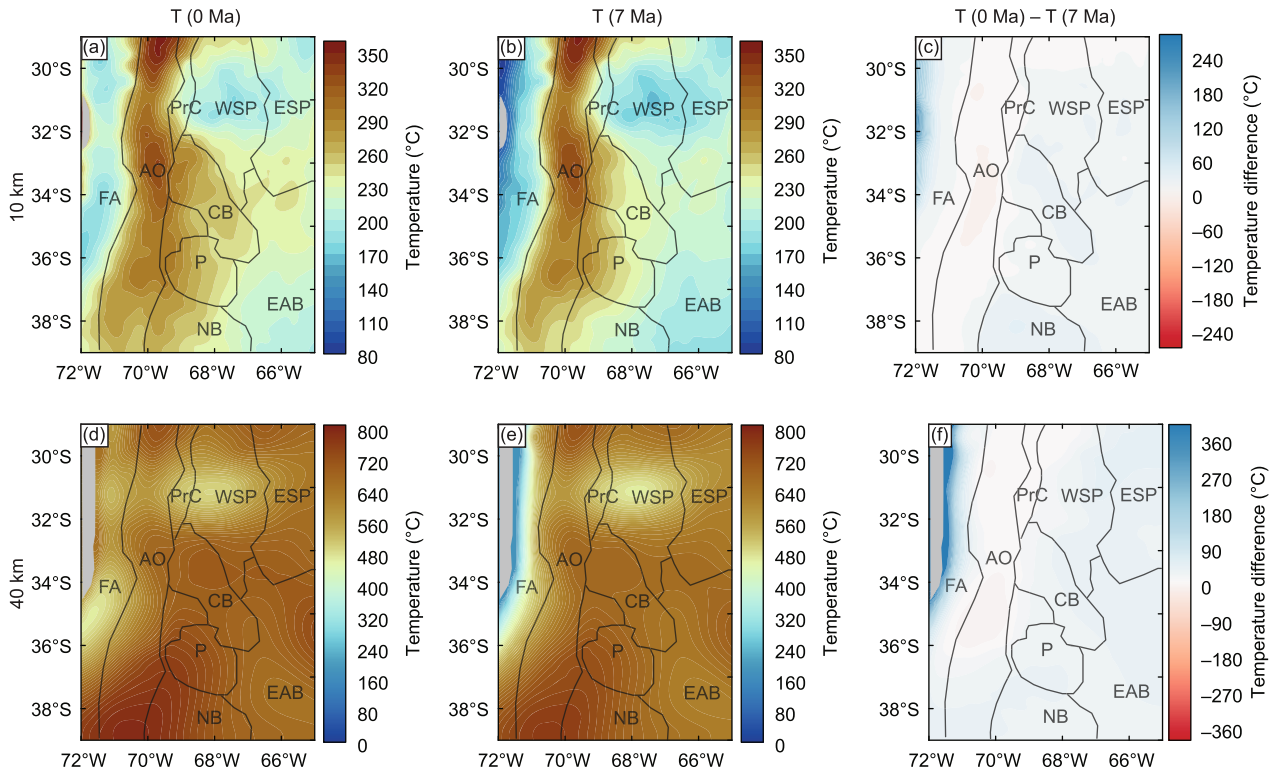


FIGURE 11: Transient temperature distribution in the overriding plate at depths of 10 and 40 km (a, b, and c), as induced by the advection at the subduction interface at 0 Ma and 7 Ma time steps. (c) and (f) show the temperature difference between (b) and (a) and (e) and (d), respectively. Grey-shaded areas mark regions within the oceanic plate, outside the domain of the transient thermal model. Boundaries of the main morphotectonic provinces are also marked with black lines. For abbreviations, see Figure 1.

representative depth slices (10 and 40 km bmsl) indicates that the largest temperature difference (up to 370 °C) is registered in a narrow band within the forearc close to the subduction interface (Figure 11). Such a difference is due to the advection of the cold thermal front along this interface. In the remaining areas, temperatures at 7 Ma are up to 10 °C higher than the initial time step due to diffusion within the thick radiogenic crust in the orogen. In view of these results and the significantly larger lateral variations in temperature at different depth levels (Figure 7), we consider the assumption of thermal equilibrium as an adequate approximation for the thermal calculations of the shallow domain of the overriding plate in the SCA.

4.1.2. Implications of Methodological Limitations on the Calculated Lithospheric Thermal Field. The model results depend on the parametrization of physical properties and boundary conditions. One source of uncertainty is related to the v_s -to-T conversion. While variations in the thermal expansion coefficient α and attenuation Q have negligible effects on the inverted thermal field, the sensitivity analysis for the v_s -to-conversion shows that using the conversion method of Priestley and McKenzie [102] yields large temperature differences with respect to the reference model (Figures 6(q)–6(t)). One has to keep in mind though that the empirical conversion method of Priestley and McKenzie [102] is associated with large uncertainties (250–360 °C) for temperatures <900 °C [100, 131], which makes the results

at shallow mantle depths highly questionable and the temperature distribution at 50 km bmsl (with reference model temperatures of mostly 400–700 °C; Figure 5(a)) a much less appropriate lower boundary condition for the performed forward thermal modelling performed.

To assess the effects of compositional variations on the derived temperature variations, we have also used the conversion method of Goes et al. [87] for two scenarios of upper mantle lherzolite variants, the reference model with a deeper garnet lherzolite modification (Table) and a spinel-only-composed alternative. The temperature difference between the reference and alternative models is only significant in a limited portion of the shallow mantle (<100 km) characterized by high v_s (>4.6 km s⁻¹), as is the case for the flat-slab segment and the forearc (Figure 6). Moreover, the regional thermal pattern in the mantle (i.e., the thermal contrast between the flat- and steep-slab segments) is a robust feature common to all model configurations despite variations in mantle composition. Temperature maps showing the difference between the two models when used as lower thermal boundary conditions for the forward thermal model are provided in the supporting information (Figure S12). Although the model with the alternative lower boundary condition predicts temperatures that are up to 80 °C higher than the reference model described in Section 3.2, the regional thermal heterogeneity remains unchanged, with contrasts between the forearc, orogen, and foreland, and between the flat- and steep-slab segments. From these observations, we

can conclude that the modeled trends in temperature variations are within the same order of magnitudes, though still within its range of uncertainty, even when considering an alternative parametrization other than the preferred v_s -to-T conversion model.

Another limitation of the v_s -to-T conversion is related to the thermal structure within the slab. Although the oceanic plate displays higher v_s and lower temperatures with respect to the surrounding mantle (e.g., Figure 5; Figure S1 in Supporting information), the modeled thermal gradient within the plate is not as large as the one predicted by other analytical or numerical approximations of the thermal structures of subduction zones [14, 141]. The strong lateral contrasts of v_s are smoothed due to the resolution of the seismic tomography. This results in lower v_s and therefore higher temperatures than the predictions of these theoretical thermal models. On the contrary, v_s and resulting temperature anomalies within the continental mantle are of larger wavelength than those of the slab; thus, they can be captured by the longer wavelength surface waves of the seismic tomography. Therefore, our discussion mostly focuses on the thermal heterogeneities of the overriding plate and subduction interface.

A third limitation is that we do not consider additional effects from partial melting and fluids in the v_s -to-T conversion. Melts in the mantle can lower seismic velocities due to an increase in anelastic relaxation [132, 133]. This effect depends mainly on the interconnection between melt pockets [134]. However, a proper quantification of this effect is hindered by inaccuracies in the estimation of the effect of anelasticity in high-temperature experiments [87, 135]. Further complexities are related to the presence of water, which would also lower the solidus and therefore would lead to an increase in the melting point [136]. Previous studies have suggested that an increase of melt fraction by 0.1 would cause a V_s decrease between 0.7% and 8.5% [87, 137], owing this range of variability to variations in melt geometry. However, the effect of these velocity variations due to partial melting on the converted temperatures below 50 km appears to be small (up to 20 °C, [138]). In the SCA, although we would expect partial melting to be somehow relevant in the subarc and forearc mantle due to the release of fluids from the oceanic plate [139], the seismic and/or geochemical information on the percentage of melt and fluids in the upper mantle (e.g., [67, 140]) is too limited to attempt any quantification of their effects on converted temperatures. We should nevertheless acknowledge that, in these areas, temperatures from seismic velocities should be interpreted with caution.

Due to its setup, the thermal modelling applied to the shallow domain (0–50 km) does not account for additional, nonconductive heat transport processes acting close to or within the subduction interface, including mantle-wedge convection and frictional shear heating [14, 130, 141–145]. For the case of viscous flow in the mantle wedge, 2D thermokinematic models of Central Chile calibrated with heat flow observations [127] indicate that this process only starts to dominate at depths larger than 80 km, which is below our

forward modelled domain. The subduction interface at shallower depths (<50 km), in contrast, is largely influenced by shear heating effects [14, 127, 141]. In an attempt to quantify this process, we used the analytical approximation of England [141] for the thermal structure of the subduction interface (Text S6 in Supporting Information). We found that considering the addition of shear heating leads to up to ~40 °C higher temperatures along the subduction interface compared to a model without this heat source (Figure S11 in Supporting Information). This effect of shear heating is small compared to the temperature decrease caused by the advection of the cold oceanic plate (Section 4.1.1); thus, we consider that it would not greatly affect the temperature trends observed in the lithosphere.

Finally, additional methodological uncertainties relate to the limited resolution, coverage, and lateral differentiation of the lithospheric units in the 3D structural model, as well as to imposed thermal properties. Although there is an inherent non-uniqueness in the way thermal properties influence the results, the range over which these properties can vary is limited (see Text S3 in the supporting information). In addition to testing the effect of end-member property values, the use of borehole temperatures in combination with a wide variety of independent lithology-constraining data sets, including seismic tomography, seismic reflection and refraction data, and gravity anomalies, helped reduce the range of property variability. Future improvement in the definition of higher-order temperature contrasts would require more densely spaced seismic experiments focused on the deep crustal structure of the SCA and more wells including also extensive temperature measurements to cross-check the modeling results. Overall, the identified first-order thermal effects proved to be robust even for tested variations in imposed properties.

4.2. Controlling Factors of the Lithospheric Thermal Field.

Our results indicate that the shallow thermal field of the lithosphere (<50 km) is largely controlled by the configuration of the continental crust, with temperatures varying according to the thickness of the sedimentary rocks and crystalline crust (Figures 7 and 9). Close to the surface (< 5 km), thick sedimentary basins (main depocenters of the Cuyo and Neuquén basins) exhibit temperatures up to ~40 °C higher than the basin margins (Figure 7). This is the effect of thermal blanketing produced by the low-conductive sedimentary layers [20, 21, 147, 148]. In contrast, the presence of thermally more conductive crystalline rocks leads to a more efficient heat transport where sedimentary cover rocks are absent and to colder shallow temperature at the same depth.

In the areas where the sedimentary units are thin (<2 km thick) or absent, the variations in the topographic relief and in the thickness of the upper continental crystalline crust exert the primary influence on the shallow thermal field. This topographic effect is related to the general increase in temperature with depth, which results in higher temperatures in the orogen than in the foreland at the same elevation. The positive correlation between thickness of the upper continental crystalline crust and higher heat budget compared to the other lithospheric layers stems from these

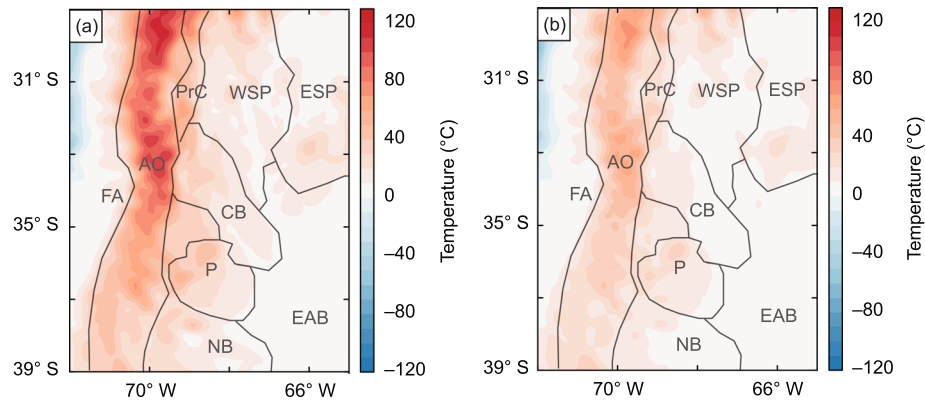


FIGURE 12: Difference between temperature distributions below sea level and below surface at depths of (a) 2 km and (b) 20 km, illustrating the topographic effect on the thermal field. Key morphotectonic provinces are shown. Refer to Figure 1 for abbreviations.

rocks being enriched in radioactive heat-producing elements due to their felsic composition [121]. These two superposed effects increase crustal temperatures in areas with high elevation (>1.5 km above mean sea level) and larger than average upper crustal thickness (>20 km). These characteristics are particularly evident in the Andean orogen, where temperatures at 2 km bmsl are up to 100 °C higher with respect to the forearc, the remaining backarc, and the foreland regions. Outside of the orogen, the average topographic elevation and the upper continental crystalline crustal thickness decrease to 700 m above mean sea level and 10 km, respectively. Consequently, the temperatures also decrease compared to the orogen at the same depth. To further examine the effects of topographic relief and upper crustal thickness on the shallow thermal field, we extracted the temperatures at 2 and 20 km below sea level ($T_{z(\text{bmsl})}$) and below surface ($T_{z(\text{topo})}$) and computed the difference between the two reference levels (T_{diff}) for each depth:

$$T_{\text{diff}} = T_{z(\text{bmsl})} - T_{z(\text{topo})} \quad (7)$$

The temperature differences at 2 km and 20 km are shown in Figure 12. We observe that at shallow depths of 2 km, the temperature differences are indeed affected by variations in the topography (~100 °C in areas of 3–6 km elevation). This effect decreases with greater depth, although it is still evident at 20 km bmsl. At this depth level, temperature differences are up to 50 °C between areas of different topographic elevation. Below 20 km bmsl, the influence of the upper crustal thickness outweighs the topographic effect.

In contrast to the shallow domains of our model, for which the parametrization of the forward thermal modelling gives direct insights into the causes of obtained thermal anomalies, we rely on a more qualitative interpretation for depths of >50 km where the thermal field is derived from seismological observations. To identify and evaluate anomalous thermal trends in the mantle of the overriding plate, we have therefore subtracted a geotherm regarded as typical for continental lithosphere [146] from the tomography-derived temperatures in this deeper model domain. This normaliza-

tion yields the volumetric extents of two major low-temperature domains: One that is known the “cold nose” (CN) along the trench and another one in the flat slab region (FS; Figure 13).

Below 50 km bmsl, we find that the lithospheric thermal field is dominantly influenced by both the cooling effect of the subducting slab and heat input from the mantle (thermally-driven mantle upwelling). The degree to which the slab dynamics affect the temperature distribution by advective cooling varies with distance from the trench and the subduction angle. The mantle of the overriding plate exhibits the lowest temperatures close to the trench, within the cold nose of the forearc, and where the slab flattens (mostly at 85 km bmsl beneath the Sierras Pampeanas). In contrast, temperatures at depths >50 km bmsl beneath the Sierras Pampeanas increase towards areas where the slab dips steeply (~30°). These results are consistent with the lower surface heat flow values observed [63, 64, 68]. Also these results are consistent with results from 2D thermomechanical modeling efforts for the area [67]. They suggest temperatures of 600 °C at the top of the flat slab (100–120 km bmsl)—a value that is consistent with the lower temperatures modeled across the subduction interface beneath the Sierras Pampeanas (Figure 13).

The spatial correlation between the temperature distribution of the overriding plate and the subduction angle breaks within the northern orogen above the flat slab between 20 and 100 km bmsl (29°–30°S and 70°–70.5°W; Figures 5, 7, and 13). In this domain, a temperature excess of up to ~250 °C is predicted along the remaining flat-slab segment (FS warm domain; Figure 13), with values similar to those of the steep-slab segment. As the subduction angle does not change, an additional forcing factor other than the subduction angle should be considered, to explain these locally elevated temperatures, a suggestion made previously, albeit not extensively discussed [80, 81]. Between 30°S and 33°S, our results indicate a spatial correlation between the thermal heterogeneity derived from the v_s -to-T conversion [83] and the configuration of the upper crust. The lowest temperatures in the subhorizontal slab segment occur where the upper crust is thin, while the highest temperatures occur

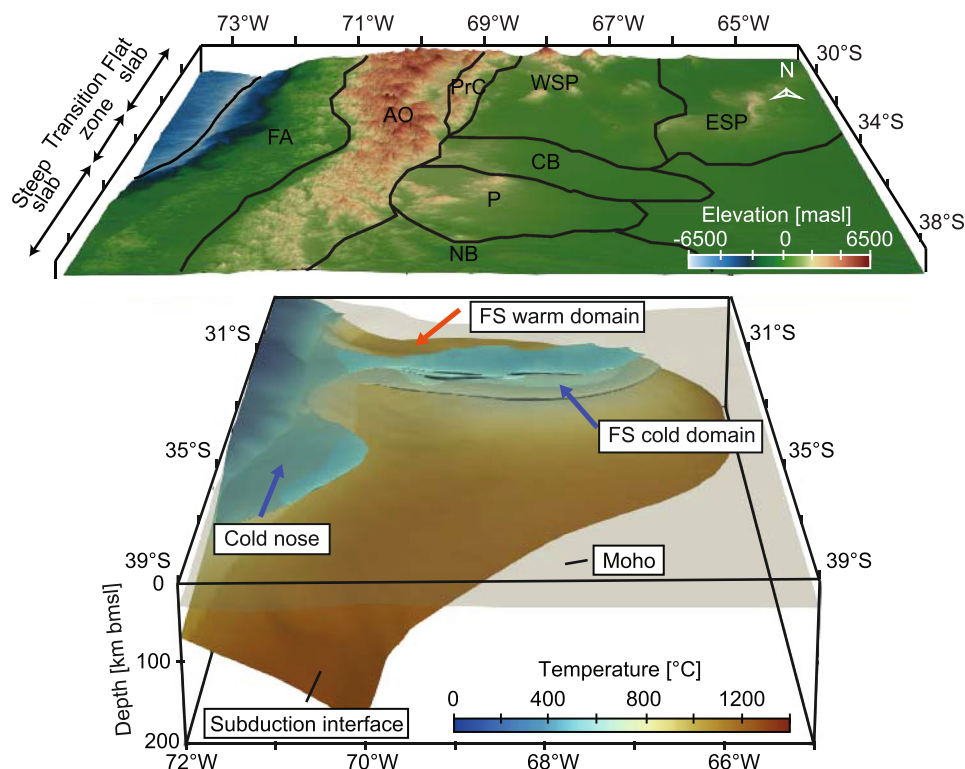


FIGURE 13: Upper panel: topography of the study region superposed with boundaries of the main morphotectonic provinces (for abbreviations see Figure 1). The extent of the subduction segments and the trench are also shown. Lower panel: temperature at the subduction interface. The 3D configuration of cold domains in the overriding plate mantle is superimposed and indicated by blue arrows. The red arrow indicates the warmest part ($\sim 1000^\circ\text{C}$) of the flat-slab segment. The extent of the Moho is shown by the beige transparent layer. FS = flat-slab.

where it thickens (cf. Figure 2(c)). This indicates that, in the warmer, northern part of the orogen, heating from a thicker upper continental crystalline crust outweighs the cooling effect of the underlying flat oceanic slab. Conversely, areas in the flat segment with a thin upper crust and a thick lower crystalline crust are significantly colder due to the smaller contribution of the lower crustal unit to the internal heat budget.

While the thick upper crust provides an explanation for low v_s (high T) below the orogen north of 30°S , the foreland of the flat-slab domain is underlain by a thinner upper crust and thus relatively high mantle temperatures (due to low v_s) there are more difficult to understand. It is likely that the resolution of the S wave tomography could have influenced the results within the latter area. North of the flat slab, high-resolution tomography [149, 150] identifies a N-S increase of v_s at 27°S with a sharp transition between low v_s below the southern Puna Plateau (that have been interpreted as resulting from delamination of the lower crust and the mantle; [151, 152]) and high v_s below the Sierras Pampeanas. Therefore, we speculate that this sharp velocity transition appears smoothed in the tomography of Assumpção et al. [83] due to its coarser resolution, resulting in lower modeled v_s , and therefore higher temperatures, in the foreland north of 30°S .

To investigate the degree of influence of mantle-related temperature variations on the shallow thermal field, we compared our results to a steady-state conductive model with a simplified lower boundary condition derived from a constant geothermal gradient of 5°C km^{-1} ([130]; Figure S13 in the supporting information), thus neglecting lateral thermal heterogeneities. At depth, there is no pronounced thermal contrast between the foreland of the flat and steep subduction segments, indicating that below 50 km bmsl, the main causative factors of the thermal heterogeneity of the foreland are the mantle heat input and the cooling effect of the slab. Moreover, the fit of the model with a simplified boundary condition and observed temperatures is decreased in which the modeled temperatures are 5°C to 80°C colder than the borehole data (Figure S14 in the supporting information). This implies that predicting the measured temperatures requires laterally variable heat input from the slab and the lithospheric mantle in addition to the heterogeneous crustal structure.

There is an ongoing debate concerning the importance of radiogenic heat production for the thermal field and the long-term evolution of orogens where the radiogenic crust is thickened and where thermal effects of shortening, exhumation, and partial melting are observed (e.g., [1, 153–156]). Some authors suggest that radiogenic heating has less

influence on the thermal field of the lithosphere in the overriding plate than either shear heating along the subduction interface [157] or episodes of magmatic underplating [158]. Yet other authors have focused on the general thermal evolution of subduction orogens and the metamorphic record, proposing that shallow asthenospheric convection is the main process responsible for elevated temperatures in the lithosphere while disregarding any significant contribution from radiogenic heat production [159]. The latter study suggests that thermal equilibrium is achieved only 50 Ma after the main shortening phase, which contradicts the observation that peak metamorphism is synchronous with thickening [160, 161]. However, the interpretations concerning thermal equilibrium conditions in orogens have recently been disputed based on results from geodynamic numerical modeling [153]. These results suggest that radioactive heating during crustal thickening is responsible for the observed marked temperature increase and subsequent partial melting within the mid-crust after 30 Ma of shortening. The present-day SCA are within this time window after the main phase of shortening, which implies that crustal thickening that has taken place over more than 30 Ma could indeed explain a significant part of excessive surface heat flow [63, 64, 72] and the low seismic velocities observed across the orogen [67, 69–71, 162].

Predicted surface heat flow varies between the high surface heat flow domains over both the orogen and the Payenia volcanic province (80–100 mWm^{-2}), and low heat flow domains over the forearc, the remaining backarc, and foreland regions (50–60 mWm^{-2} and 40–70 mWm^{-2} , respectively; Figures 8 and 9). These surface heat flow variations correlate spatially with the thickness configuration of the sedimentary strata and upper crystalline crust: high heat flow in areas with thin or absent low-conductive sedimentary rocks and thick radiogenic upper crust (i.e., Andean orogen, Payenia volcanic province) and low heat flow in regions with thick sedimentary cover and/or thin upper crust (foreland basins, forearc). Mantle-source contributions are found to play a less dominant role on surface heat flow than the abovementioned shallow structures. In the foreland regions, mantle heat flow reaching the base of the crust (Moho) is $\sim 40\%$ of the surface heat flow, whereas this contribution decreases down to 20–30% in the orogen (Figure S15 in supporting information). In contrast, the forearc is characterized by 60% of contribution from mantle heat flow to the surface heat flow, which is likely related to the absence of a thick upper crust and to the shallow underlying cold slab.

The observed trends between low and high surface heat flow in the forearc orogen is in agreement with results from 2D generic models of subduction zones [127, 163, 164]. The model of Wada and Wang [127] across a profile lying in the steep-slab region, however, predicts an overall lower heat flow than our model (50–75 mWm^{-2} vs. 75–90 mWm^{-2} Figure 8(c)). Colder conditions are likely due to differences in the model assumptions. Their model considers a lower radiogenic heat production of the upper continental crust than ours (1.3 μWm^{-3} vs. 2 μWm^{-3}), which translates in higher temperatures, thus higher surface heat flow in our model. Additionally, the 2D model of Wada and Wang

[127] does not consider lateral heat input and transport perpendicular to the 2D profile which could lead to an overall lower heat budget.

The effects of the spatially variable heat input (either from the deep mantle or from radiogenic sources) and variably efficient heat conduction demonstrate that the surface heat flow alone is a poor proxy for lower crustal or lithosphere thickness [20]. Nevertheless, heat flow estimates are often compared to seismic tomography, where S wave attenuation (Q_s) anomalies correlate to some extent with the thermal field [165]. While areas of high heat flow are usually related to low Q_s (high attenuation of the v_s), low heat flow is commonly associated with colder areas and hence high Q_s (low attenuation of v_s). These spatial correlations were also identified across the SCA. Between 31.5°S and 33.5°S, high surface heat flow predicted for the orogen coincides with low Q_s (650–670; [166]). Accordingly, low predicted heat flow correlates with high Q_s (800–1050) in the forearc and the foreland [166].

Discrepancies between observed surface heat flow [63, 68, 126] and the steady-state conductive model predictions in the proximity of active volcanic centers (Figures 8 and 10(d)) can certainly be related to unconsidered transient advective heat transport processes, such as fluid migration or the existence of melts (e.g., [20, 167] and references therein). For instance, unconsidered effects of magma flow beneath the active volcanic arc can result in a local temperature increase of up to 200 °C [167]. González-Vidal et al. (2018) demonstrated that such local effects of partial melting can be interpreted from negative S wave anomalies imaged below the southern volcanic arc in the SCA area.

4.3. Implications of the Thermal Field for the Deformation Modes in the SCA. In view of the sensitivity of rock rheology to temperature, the lithological configuration from Rodríguez Picada et al. [58] and temperature variations derived in this study can be analyzed qualitatively in terms of their implications for the long-term strength of the lithosphere. In particular, areas that are colder and of more mafic lithology (i.e., the northern part of the forearc and foreland) are potentially stronger and can withstand higher levels of horizontal stresses before deforming viscously [168] compared to areas that are warm and more felsic in composition (i.e., the orogen, the Payenia volcanic province, and the foreland at the latitudes of the transition to the steeper subduction segment).

The general trends in the modeled temperature distribution of the SCA lithosphere are consistent with independent elastic-thickness estimates derived from flexure analysis of the gravity field, which are an alternative, indirect proxy of lithospheric strength [25, 78, 80, 169, 170]. High and low elastic thickness are indicative of a strong and weak lithosphere, respectively [171, 172]. In the SCA, areas of high elastic thickness (40–60 km) correlate spatially with the modeled cold forearc and the northern part of the foreland. Conversely, areas of low elastic thickness (< 30 km) correlate spatially with the modeled warm areas of the orogen, the Payenia volcanic province, and the foreland at the latitude of the transition to the steeper subduction segment.

The inferred trends in lithospheric strength related to variations in the upper-plate configuration have strong implications for the long-term deformation processes of the Central Andes [4, 8, 173, 174]. For example, Barrionuevo et al. [4] argued on the basis of geodynamic numerical modeling that the vergence of the orogenic wedge at 33°–36°S is mainly controlled by the E-W-oriented asymmetry of the lithosphere-asthenosphere boundary (LAB). The LAB configuration proposed by these authors agrees with our study, where a warmer lithospheric mantle, and thus shallower thermal LAB, is encountered beneath the orogen compared to the adjacent foreland and forearc, i.e., areas where the mantle is colder and the LAB is located at greater depth. Furthermore, Barrionuevo et al. [4] suggest that heterogeneities in continental crustal composition could explain the observed N-S-oriented variations in the amounts of shortening and its spatial distribution within the orogen and the foreland between 33° and 36°S. In the orogen north of their study region, the upper and lower crustal deformation maxima are aligned vertically with the strongest overall crustal thickening (pure-shear or coupled deformation mode), whereas to the south, upper crustal deformation is horizontally displaced with respect to the locus of lower crustal deformation (simple-shear or decoupled deformation mode). Pure-shear deformation at 33°S would be mainly related to a more felsic and weaker crust; in contrast, simple-shear deformation at 36°S would result from a mafic and stronger crust [4]. These results are compatible with gravity-constrained density distributions in the crust in the same region as proposed by Rodríguez Piceda et al. [58] and with our results of an N-to-S-oriented decrease in crustal temperatures.

Furthermore, our results provide new aspects for the controversial debate over the governing mechanisms responsible for the spatially disparate thick-skinned deformation in the broken-foreland provinces of the Sierras Pampeanas between 27° and 33°S and the Santa Bárbara System farther north. While some authors have proposed that the flat slab is responsible for the thick-skinned deformation [26, 175, 176], others have argued that this style of deformation is controlled by the reactivation of crustal heterogeneities prior to slab flattening such as Paleozoic sutures and associated deformation fabrics between crustal terranes or the inversion of Cretaceous normal faults [6, 38, 41, 43, 174, 177–181]. In the case, that the flat slab is responsible, the concept of “bulldozed keel” was suggested, which means that the oceanic plate continuously transfers tectonic stresses to the front of the flat segment where the slab is already steep [26, 74, 175, 182]. In this scenario, however, the role of the thermal field and the rheology of the overriding plate in the transmission and localization of stresses is not taken into account. Martinod et al. [176] argue that the lithosphere above the flat slab is a subject to minor deformation because it is colder and stronger. Therefore, deformation localizes where the slab starts to resume its steep subduction angle, triggered by slab-pull forces, rather than where the slab is already steep, as proposed by the “bulldozed-keel” models [26, 74, 175, 182]. Our results support the hypothesis of Martinod et al. [176] in that the mafic crust and cold litho-

sphere beneath the Sierras Pampeanas suggest that the lithosphere there is strong. This may therefore inhibit the formation of crustal-scale faults, thus dismissing the “bulldozed keel” effect as an efficient mechanism for propagating deformation. Instead, the localization of deformation in the Sierras Pampeanas could be due to either mechanical weakening within inherited basement heterogeneities and/or increased slab-pull where the slab resumes steep subduction. In summary, the results of our study support the hypothesis that inherited rheological heterogeneities and/or slab steepening controlled the geometry of faults that delimit the spatially isolated basement uplifts and the intervening sedimentary basins of the broken foreland between 27°S and 33°S, rather than slab flattening. Discriminating between these hypotheses ultimately requires additional geodynamic modeling applied to the case of the SCA.

On the basis of geodynamic numerical modeling, it has been proposed earlier that the strength of the overriding plate sustained the flat subduction setting of the oceanic plate over the last ~20 Ma [56, 57, 59]. This has been suggested to be the case for the northern part of the SCA (27°–33°S), where the subhorizontal slab segment underlies the thick and dense crust of the foreland of the South American plate [58]. Interestingly, the cold temperatures modeled for this area in our study exhibit two effects that might also favor slab shallowing: (i) cooling of the subduction interface that enhances the coupling between the continental and oceanic plates and (ii) efficient E-W stress transmission along the cold and strong overriding plate, which forces the trench to retreat. In this context, there is a positive feedback between the cold lithosphere in the northern foreland and the flat subduction setting: The shallow slab, together with a thin radiogenic crust, would cause low temperatures in the lithosphere in this domain, thereby strengthening the overriding plate, which in turn would promote slab shallowing.

5. Conclusions

By combining conversion of *S* wave seismic tomography to temperatures and steady-state conductive numerical modeling, we derived the 3D lithospheric-scale temperature distribution of the southern Central Andes and adjacent forearc and foreland regions and conclude the following:

- (1) Distinct controlling factors of the thermal field are dominant at different depths. At shallow depths (<50 km bmsl), the thermal contrast between the warm orogen and the relatively cold areas of the forearc and foreland is modulated by the thickness of the upper radiogenic continental crystalline crust, which generates lateral changes of heat production. In the uppermost levels (< 5 km), the effect of the sediment thickness is superimposed, leading to depocenters of the foreland basins being warmer than the edges due to thermal blanketing. The cool oceanic slab outweighs the heating effect of the continental crust in regions with relatively shallow slab depth (<85 km bmsl) and where the upper

continental crystalline crust is thin. This occurs in the forearc and in most of the northern part of the foreland (29°–33°S) where the slab flattens. At depths of >50 km bmsl, the spatial correlation between crustal features and thermal heterogeneities is insignificant, and the mantle heat flow and the effect of the cold slab become the main controlling factors. However, down to 100 km bmsl, temperatures are additionally affected by the radiogenic contribution of the upper continental crystalline crust in the northern part of the orogen where this unit has a significant thickness (>30 km)

There exists a strong contrast in surface heat flow between the warm orogen (80–105 mWm⁻²) and the relatively cold forearc and foreland areas (40–75 mWm⁻²). These variations in heat flow are primarily controlled by the thickness configuration of the uppermost layers (sediments and upper crystalline crust). The shallow cold slab affects the pattern of surface heat flow beneath the forearc

- (2) The modeled temperature configuration has implications for the rheology and, therefore, deformation patterns of the SCA. A cold, mafic, thick, and therefore potentially strong lithosphere beneath the broken foreland of the Sierras Pampeanas is prone to deformation processes that are controlled by inherited heterogeneities in the upper plate or by slab-pull, where the oceanic plate resumes steep subduction. In addition, such a lithospheric configuration may favor the coupling between the subducting and overriding plates, potentially contributing to a flat subduction setting
- (3) Sensitivity analysis of the v_s -to-T conversion shows that, at depths of <100 km, mantle composition has the strongest effect on the v_s -to-T conversion for v_s larger than 4.6 km s⁻¹, as is the case for the flat-slab segment. Nevertheless, compositional variations within the range of uncertainty do not significantly affect the main temperature and heat flow trends found in the tomographically studied mantle

Data Availability

The 3D thermal model presented in this publication can be accessed via GFZ Data Services (doi:10.5880/GFZ.4.5.2021.001).

Conflicts of Interest

The authors declare that they have no conflicts of interest.

Acknowledgments

This research was funded by the Deutsche Forschungsgemeinschaft (DFG) and the Federal State of Brandenburg under the auspices of the International Research Training Group IGK2018 “SuRfAce processes, TECTonics and Georesources: The Andean foreland basin of Argentina” (STRAT-

EGy), DFG grant STR 373/34-1 to M. Strecker and M. Scheck-Wenderoth. We are grateful to Marcelo Assumpção and Mei Feng for providing the seismic tomography for the conversion to temperatures and to Corinna Kallich for the assistance on the figures. The color scales were taken from Cramer (2018), scientific color maps (doi:10.5281/zenodo.1243862). Data visualization was carried out with ParaView software (<https://paraview.org>). Figures were produced with Python.

Supplementary Materials

The supporting information includes the following: (i) Representative depth slices of the S wave tomography used to convert velocities to temperatures (v_s -to-T conversion, Figure S1). (ii) A description of the sensitivity analysis of the v_s -to-T conversion (Text S1, Figures S2 and S3). (iii) The workflow followed to assign thermal properties to each layer of the 3D structural model for the steady-state conductive thermal field calculation (Text S2, Figure S4). (iv) A description of the sensitivity analysis of the steady-state conductive thermal field calculation (Text S3, Table S1, Figures S5 and S6). (v) The upper boundary condition for computing the steady-state conductive thermal field (Text S4). (vi) The comparison between temperatures along the subduction interface predicted by our model and 2D kinematic-dynamic models of Syracuse et al. [130] (Figure S7). (vii) The calculation of surface heat flow (Text S5). (viii) The workflow followed for the transient thermal field calculation (Text S6, Figures S8–S10). (ix) The workflow followed to compute the temperature effect of shear heating in the shallow subduction interface (Text S7, Table S3, Figure S11). (x) Difference maps between temperature slices calculated using a lower boundary condition from the v_s -to-T conversion and assuming spinel and garnet lherzolite compositions to show the effect of uncertainties on the mantle composition in the uppermost lithospheric temperatures (Figure S12). (xi) Temperature slices and a comparison with thermal observations of a model using an alternative lower boundary condition to show the influence of the mantle and the slab in the uppermost lithospheric temperatures (Figures S13 and S14). (xii) The heat flow at the Moho surface and the contribution of mantle heat flow to the surface heat flow (Figure S15). (*Supplementary Materials*)

References

- [1] J.-C. Mareschal and C. Jaupart, “Radiogenic heat production, thermal regime and evolution of continental crust,” *Moho*, vol. 609, pp. 524–534, 2013.
- [2] D. L. Turcotte and G. Schubert, *Geodynamics*, Cambridge University Press, 2012.
- [3] R. W. Allmendinger and T. Gubbels, “Pure and simple shear plateau uplift, Altiplano-Puna, Argentina and Bolivia,” *Tectonophysics*, vol. 259, no. 1–3, pp. 1–13, 1996.
- [4] M. Barrionuevo, S. Liu, J. Mescua et al., “The influence of variations in crustal composition and lithospheric strength on the evolution of deformation processes in the southern Central Andes: insights from geodynamic models,” *International Journal of Earth Sciences*, vol. 110, no. 7, pp. 2361–2384, 2021.

- [5] F. Ibarra, C. B. Prezzi, J. Bott, M. Scheck-Wenderoth, and M. R. Strecker, "Distribution of temperature and strength in the Central Andean lithosphere and its relationship to seismicity and active deformation," *Journal of Geophysical Research: Solid Earth*, vol. 126, no. 5, 2021.
- [6] J. Kley, C. R. Monaldi, and J. A. Salfity, "Along-strike segmentation of the Andean foreland: causes and consequences," *Tectonophysics*, vol. 301, no. 1-2, pp. 75–94, 1999.
- [7] N. J. Kusznir and R. G. Park, "Intraplate lithosphere deformation and the strength of the lithosphere," *Geophysical Journal International*, vol. 79, no. 2, pp. 513–538, 1984.
- [8] S. Liu, "Controls of foreland-deformation patterns in the orogen-foreland shortening system," 2020, 2020, <https://publishup.uni-potsdam.de/frontdoor/index/index/docId/44573>.
- [9] S. Goes, D. Hasterok, D. L. Schutt, and M. Klöcking, "Continental lithospheric temperatures: a review," *Physics of the Earth and Planetary Interiors*, vol. 306, p. 106509, 2020.
- [10] S. M. Peacock, "Advances in the thermal and petrologic modeling of subduction zones," *Geosphere*, vol. 16, no. 4, pp. 936–952, 2020.
- [11] K. Boonma, A. Kumar, D. Garcia-Castellanos, I. Jiménez-Munt, and M. Fernández, "Lithospheric mantle buoyancy: the role of tectonic convergence and mantle composition," *Scientific Reports*, vol. 9, no. 1, p. 17953, 2019.
- [12] H. Čížková and C. R. Bina, "Effects of mantle and subduction-interface rheologies on slab stagnation and trench rollback," *Earth and Planetary Science Letters*, vol. 379, pp. 95–103, 2013.
- [13] F. Garel, S. Goes, D. R. Davies, J. H. Davies, S. C. Kramer, and C. R. Wilson, "Interaction of subducted slabs with the mantle transition-zone: a regime diagram from 2-D thermo-mechanical models with a mobile trench and an overriding plate," *Geochemistry, Geophysics, Geosystems*, vol. 15, no. 5, pp. 1739–1765, 2014.
- [14] P. E. van Keken, I. Wada, N. Sime, and G. A. Abers, "Thermal structure of the forearc in subduction zones: a comparison of methodologies," *Geochemistry, Geophysics, Geosystems*, vol. 20, no. 7, pp. 3268–3288, 2019.
- [15] J. Rodríguez-González, A. M. Negrodo, and M. I. Billen, "The role of the overriding plate thermal state on slab dip variability and on the occurrence of flat subduction," *Geochemistry, Geophysics, Geosystems*, vol. 13, no. 1, 2012.
- [16] R. L. Rudnick and S. Gao, "3.01- composition of the continental crust," in *Treatise on Geochemistry*, H. D. Holland and K. K. Turekian, Eds., pp. 1–64, Pergamon, Oxford, 2003.
- [17] S. R. Taylor, "The origin and growth of continents," *Tectonophysics*, vol. 4, no. 1, pp. 17–34, 1967.
- [18] J. Freyemark, J. Sippel, M. Scheck-Wenderoth et al., "The deep thermal field of the Upper Rhine Graben," *Tectonophysics*, vol. 694, pp. 114–129, 2017.
- [19] M. K. Kaban, M. Tesauero, W. D. Mooney, and S. A. P. L. Cloetingh, "Density, temperature, and composition of the North American lithosphere-new insights from a joint analysis of seismic, gravity, and mineral physics data: 1. Density structure of the crust and upper mantle," *Geochemistry, Geophysics, Geosystems*, vol. 15, no. 12, pp. 4781–4807, 2014.
- [20] M. Scheck-Wenderoth, M. Cacace, Y. P. Maystrenko et al., "Models of heat transport in the Central European Basin System: effective mechanisms at different scales," *Marine and Petroleum Geology*, vol. 55, pp. 315–331, 2014.
- [21] J. Sippel, C. Meeßen, M. Cacace et al., "The Kenya rift revisited: insights into lithospheric strength through data-driven 3-D gravity and thermal modelling," *Solid Earth*, vol. 8, no. 1, pp. 45–81, 2017.
- [22] C. Spooner, M. Scheck-Wenderoth, M. Cacace, H.-J. Götze, and E. Luijendijk, "The 3D thermal field across the Alpine orogen and its forelands and the relation to seismicity," *Global and Planetary Change*, vol. 193, p. 103288, 2020.
- [23] M. Tesauero, M. K. Kaban, and S. A. P. L. Cloetingh, "How rigid is Europe's lithosphere?," *Geophysical Research Letters*, vol. 36, no. 16, 2009.
- [24] D. Anikiev, M. Cacace, J. Bott, M. L. Gomez Dacal, and M. Scheck-Wenderoth, "Influence of lithosphere rheology on seismicity in an intracontinental rift: the case of the Rhine Graben," *Frontiers in Earth Science*, vol. 8, p. 492, 2020.
- [25] F. Ibarra and C. B. Prezzi, "The thermo-mechanical state of the Andes in the Altiplano-Puna region: insights from curie isotherm and effective elastic thickness determination," *Revista de la Asociación Geológica Argentina*, vol. 76, no. 4, pp. 352–362, 2019.
- [26] T. E. Jordan, B. L. Isacks, R. W. Allmendinger, J. A. Brewer, V. A. Ramos, and C. J. Ando, "Andean tectonics related to geometry of subducted Nazca plate," *Geological Society of America Bulletin*, vol. 94, no. 3, pp. 341–361, 1983.
- [27] C. Mpodozis and V. Ramos, "The Andes of Chile and Argentina," in *Geology of the Andes and its Relation to Hydrocarbon and Mineral Resources*, pp. 59–90, Earth Sciences Series, Houston, TX, USA, 1990.
- [28] R. Astini, J. Benedetto, and N. Vaccari, "The early Paleozoic evolution of the Argentine Precordillera as a Laurentian rifted, drifted, and collided terrane: a geodynamic model," *Geological Society of America Bulletin*, vol. 107, no. 3, pp. 253–273, 1995.
- [29] C. Azcuy and R. Caminos, "El Sistema Carbonífero en la República Argentina. Diastrofismo," in *El sistema carbonífero en la República Argentina*, pp. 239–251, Academia Nacional de Ciencias, Córdoba, Argentina, 1987.
- [30] L. B. Giambiagi, V. A. Ramos, E. Godoy, P. P. Alvarez, and S. Orts, "Cenozoic deformation and tectonic style of the Andes, between 33° and 34° south latitude," *Tectonics*, vol. 22, no. 4, 2003.
- [31] S. M. Kay, W. M. Burns, P. Copeland, and O. Mancilla, "Upper cretaceous to Holocene magmatism and evidence for transient Miocene shallowing of the Andean subduction zone under the northern Neuquén Basin," in *Evolution of an Andean Margin: A Tectonic and Magmatic View from the Andes to the Neuquén Basin (35°–39°S lat) (Vol. 407, p. 0)*, S. M. Kay and V. A. Ramos, Eds., pp. 19–60, Geological Society of America, 2006.
- [32] E. J. Llambias and A. M. Sato, "El Batolito de Colangüil (29–31° S) cordillera frontal de Argentina: estructura y marco tectónico," *Andean Geology*, vol. 17, no. 1, pp. 89–108, 1990.
- [33] E. J. Llambias, L. E. Kleiman, and J. A. Salvarredi, "El magmatismo gondwánico," in *Presented at the Geología y Recursos Naturales de Mendoza*, V. Ramos, Ed., pp. 53–64, Congreso Geológico Argentino, 1993.
- [34] C. Mpodozis and S. M. Kay, "Provincias magmáticas ácidas y evolución tectónica de Gondwana: Andes chilenos (28–31 S)," *Andean Geology*, vol. 17, no. 2, pp. 153–180, 1990.
- [35] V. A. Ramos, M. Cegarra, and E. Cristallini, "Cenozoic tectonics of the High Andes of west-central Argentina (30–36

- S latitude),” *Tectonophysics*, vol. 259, no. 1–3, pp. 185–200, 1996.
- [36] D. Boyce, R. Charrier, and M. Farías, “The first Andean compressive tectonic phase: Sedimentologic and structural analysis of mid-cretaceous deposits in the Coastal Cordillera, Central Chile (32°50’S),” *Tectonics*, vol. 39, no. 2, 2020.
- [37] L. M. Fennell, A. Folguera, M. Naipauer et al., “Cretaceous deformation of the southern Central Andes: synorogenic growth strata in the Neuquén group (35° 30’–37° S),” *Basin Research*, vol. 29, pp. 51–72, 2017.
- [38] J. Kley and C. R. Monaldi, “Tectonic inversion in the Santa Barbara System of the central Andean foreland thrust belt, northwestern Argentina,” *Tectonics*, vol. 21, no. 6, 2002.
- [39] O. Oncken, G. Chong, G. Franz et al., *The Andes: Active Subduction Orogeny*, Springer, 1st edition, 2006.
- [40] G. Yáñez and J. Cembrano, “Role of viscous plate coupling in the late Tertiary Andean tectonics,” *Journal of Geophysical Research: Solid Earth*, vol. 109, no. B2, 2004.
- [41] C. del Papa, F. Hongn, J. Powell et al., “Middle Eocene-Oligocene broken-foreland evolution in the Andean Calchaqui Valley, NW Argentina: insights from stratigraphic, structural and provenance studies,” *Basin Research*, vol. 25, no. 5, pp. 574–593, 2013.
- [42] B. L. Isacks, “Uplift of the Central Andean Plateau and bending of the Bolivian Orocline,” *Journal of Geophysical Research: Solid Earth*, vol. 93, no. B4, pp. 3211–3231, 1988.
- [43] V. A. Ramos, E. O. Cristallini, and D. J. Pérez, “The Pampean flat-slab of the Central Andes,” *Flat-Slab Subduction in the Andes*, vol. 15, no. 1, pp. 59–78, 2002.
- [44] M. Barazangi and B. L. Isacks, “Spatial distribution of earthquakes and subduction of the Nazca plate beneath South America,” *Geology*, vol. 4, no. 11, pp. 686–692, 1976.
- [45] T. Cahill and B. L. Isacks, “Seismicity and shape of the subducted Nazca Plate,” *Journal of Geophysical Research*, vol. 97, no. B12, p. 17503, 1992.
- [46] K. T. Maloney, G. L. Clarke, K. A. Klepeis, and L. Quevedo, “The late Jurassic to present evolution of the Andean margin: drivers and the geological record,” *Tectonics*, vol. 32, no. 5, pp. 1049–1065, 2013.
- [47] R. E. Jones, J. C. De Hoog, L. A. Kirstein et al., “Temporal variations in the influence of the subducting slab on Central Andean arc magmas: evidence from boron isotope systematics,” *Earth and Planetary Science Letters*, vol. 408, pp. 390–401, 2014.
- [48] R. E. Jones, L. A. Kirstein, S. A. Kasemann et al., “Geodynamic controls on the contamination of Cenozoic arc magmas in the southern Central Andes: insights from the O and Hf isotopic composition of zircon,” *Geochimica et Cosmochimica Acta*, vol. 164, pp. 386–402, 2015.
- [49] R. E. Jones, L. A. Kirstein, S. A. Kasemann et al., “The role of changing geodynamics in the progressive contamination of late cretaceous to Late Miocene arc magmas in the southern Central Andes,” *Lithos*, vol. 262, pp. 169–191, 2016.
- [50] S. M. Kay and C. Mpodozis, “Magmatism as a probe to the Neogene shallowing of the Nazca plate beneath the modern Chilean flat-slab,” *Journal of South American Earth Sciences*, vol. 19, 2002.
- [51] M.-A. Gutscher, “Andean subduction styles and their effect on thermal structure and interplate coupling,” *Journal of South American Earth Sciences*, vol. 15, no. 1, pp. 3–10, 2002.
- [52] G. A. Yáñez, C. R. Ranero, R. von Huene, and J. Díaz, “Magnetic anomaly interpretation across the southern central Andes (32–34 S): the role of the Juan Fernández ridge in the late tertiary evolution of the margin,” *Journal of Geophysical Research: Solid Earth*, vol. 106, no. B4, pp. 6325–6345, 2001.
- [53] J. van Hunen, A. P. van den Berg, and N. J. Vlaar, “A thermo-mechanical model of horizontal subduction below an overriding plate,” *Earth and Planetary Science Letters*, vol. 182, no. 2, pp. 157–169, 2000.
- [54] N. G. Cerpa, R. Hassani, M. Gerbault, and J.-H. Prévost, “A fictitious domain method for lithosphere-asthenosphere interaction: application to periodic slab folding in the upper mantle,” *Geochemistry, Geophysics, Geosystems*, vol. 15, no. 5, pp. 1852–1877, 2014.
- [55] W. P. Schellart and V. Strak, “Geodynamic models of short-lived, long-lived and periodic flat slab subduction,” *Geophysical Journal International*, vol. 226, no. 3, pp. 1517–1541, 2021.
- [56] J. Hu, L. Liu, A. Hermsillo, and Q. Zhou, “Simulation of late Cenozoic south American flat-slab subduction using geodynamic models with data assimilation,” *Earth and Planetary Science Letters*, vol. 438, pp. 1–13, 2016.
- [57] V. C. Manea, M. Pérez-Gussinyé, and M. Manea, “Chilean flat slab subduction controlled by overriding plate thickness and trench rollback,” *Geology*, vol. 40, no. 1, pp. 35–38, 2012.
- [58] C. Rodríguez Picada, M. Scheck Wenderoth, M. L. Gomez Dacal, J. Bott, C. B. Prezzi, and M. R. Strecker, “Lithospheric density structure of the southern Central Andes constrained by 3D data-integrative gravity modelling,” *International Journal of Earth Sciences*, vol. 110, no. 7, pp. 2333–2359, 2021.
- [59] W. Sharples, M. A. Jadamec, L. N. Moresi, and F. A. Capitano, “Overriding plate controls on subduction evolution,” *Journal of Geophysical Research: Solid Earth*, vol. 119, no. 8, pp. 6684–6704, 2014.
- [60] C. Amante and B. Eakins, *ETOPO1 1 Arc-Minute Global Relief Model: Procedures, Data Sources and Analysis (NOAA Technical Memorandum NESDIS NGDC-24)*, National Geophysical Data Center, 2009.
- [61] G. P. Hayes, G. L. Moore, D. E. Portner et al., “Slab 2, a comprehensive subduction zone geometry model,” *Science*, vol. 362, no. 6410, pp. 58–61, 2018.
- [62] Global Volcanism Program, *Volcanoes of the World (Version v. 4.10.5)*, Smithsonian Institution, 2013.
- [63] V. M. Hamza and M. Muñoz, “Heat flow map of South America,” *Geothermics*, vol. 25, no. 6, pp. 599–646, 1996.
- [64] V. M. Hamza, F. J. S. S. Dias, A. J. L. Gomes, and Z. G. D. Terceros, “Numerical and functional representations of regional heat flow in South America,” *Physics of the Earth and Planetary Interiors*, vol. 152, no. 4, pp. 223–256, 2005.
- [65] J. Van Hunen, A. P. Van Den Berg, and N. J. Vlaar, “On the role of subducting oceanic plateaus in the development of shallow flat subduction,” *Tectonophysics*, vol. 352, no. 3–4, pp. 317–333, 2002.
- [66] J. van Hunen, A. P. van den Berg, and N. J. Vlaar, “Various mechanisms to induce present-day shallow flat subduction and implications for the younger earth: a numerical parameter study,” *Physics of the Earth and Planetary Interiors*, vol. 146, no. 1–2, pp. 179–194, 2004.
- [67] M. Marot, T. Monfret, M. Gerbault, G. Nolet, G. Ranalli, and M. Pardo, “Flat versus normal subduction zones: a comparison based on 3-D regional traveltimes tomography and

- petrological modelling of central Chile and western Argentina (29°–35°S),” *Geophysical Journal International*, vol. 199, no. 3, pp. 1633–1654, 2014.
- [68] S. Uyeda and T. Watanabe, “Terrestrial heat flow in western South America,” *Tectonophysics*, vol. 83, no. 1–2, pp. 63–70, 1982.
- [69] L. Wagner, S. Beck, G. Zandt, and M. Ducea, “Depleted lithosphere, cold, trapped asthenosphere, and frozen melt puddles above the flat slab in central Chile and Argentina,” *Earth and Planetary Science Letters*, vol. 245, no. 1–2, pp. 289–301, 2006.
- [70] L. S. Wagner, S. Beck, and G. Zandt, “Upper mantle structure in the south central Chilean subduction zone (30° to 36°S),” *Journal of Geophysical Research: Solid Earth*, vol. 110, no. B1, 2005.
- [71] K. M. Ward, R. C. Porter, G. Zandt et al., “Ambient noise tomography across the Central Andes,” *Geophysical Journal International*, vol. 194, no. 3, pp. 1559–1573, 2013.
- [72] V. M. Hamza, R. R. Cardoso, and C. F. Ponte Neto, “Spherical harmonic analysis of earth’s conductive heat flow,” *International Journal of Earth Sciences*, vol. 97, no. 2, pp. 205–226, 2008.
- [73] V. C. Manea, M. Manea, L. Ferrari et al., “A review of the geodynamic evolution of flat slab subduction in Mexico, Peru, and Chile,” *Tectonophysics*, vol. 695, pp. 27–52, 2017.
- [74] M. Gutscher, W. Spakman, H. Bijwaard, and E. R. Engdahl, “Geodynamics of flat subduction: seismicity and tomographic constraints from the Andean margin,” *Tectonics*, vol. 19, no. 5, pp. 814–833, 2000.
- [75] S. G. Henry and H. N. Pollack, “Terrestrial heat flow above the Andean subduction zone in Bolivia and Peru,” *Journal of Geophysical Research: Solid Earth*, vol. 93, no. B12, pp. 15153–15162, 1988.
- [76] V. C. Manea and M. Manea, “Flat-slab thermal structure and evolution beneath central Mexico,” *Pure and Applied Geophysics*, vol. 168, no. 8–9, pp. 1475–1487, 2011.
- [77] C. Prezzi, M. P. Iglesia Llanos, H.-J. Götze, and S. Schmidt, “Thermal and geodynamic contributions to the elevation of the Altiplano–Puna plateau,” *Physics of the Earth and Planetary Interiors*, vol. 237, pp. 51–64, 2014.
- [78] A. Astort, B. Colavitto, L. Sagripanti et al., “Crustal and mantle structure beneath the Southern Payenia Volcanic Province using gravity and magnetic data,” *Tectonics*, vol. 38, no. 1, pp. 144–158, 2019.
- [79] G. Collo, M. Ezpeleta, F. M. Dávila et al., “Basin thermal structure in the Chilean-Pampean flat subduction zone,” in *The Evolution of the Chilean-Argentinean Andes*, pp. 537–564, Springer, 2018.
- [80] M. A. Sánchez, J. P. Ariza, H. P. García et al., “Thermo-mechanical analysis of the Andean lithosphere over the Chilean-Pampean flat-slab region,” *Journal of South American Earth Sciences*, vol. 87, pp. 247–257, 2018.
- [81] M. A. Sánchez, H. P. García, G. Acosta et al., “Thermal and lithospheric structure of the Chilean-Pampean flat-slab from gravity and magnetic data,” in *Andean Tectonics*, pp. 487–507, Elsevier, 2019.
- [82] M. E. Sigismondi, *Estudio de la deformación litosférica de la cuenca Neuquina: estructura termal, datos de gravedad y sísmica de reflexión*, Universidad de Buenos Aires Facultad de Ciencias Exactas y Naturales, 2012.
- [83] M. Assumpção, M. Feng, A. Tassara, and J. Julià, “Models of crustal thickness for South America from seismic refraction, receiver functions and surface wave tomography,” *Tectonophysics*, vol. 609, pp. 82–96, 2013.
- [84] C. Heine, *Formation and Evolution of Intracontinental Basins*, University of Sidney, 2007.
- [85] E. S. Ince, F. Barthelmes, S. Reißland et al., “ICGEM – 15 years of successful collection and distribution of global gravitational models, associated services, and future plans,” *Earth System Science Data*, vol. 11, no. 2, pp. 647–674, 2019.
- [86] J. F. Mescua, L. Giambiagi, M. Barrionuevo et al., “Basement composition and basin geometry controls on upper-crustal deformation in the Southern Central Andes (30–36°S),” *Geological Magazine*, vol. 153, no. 5–6, pp. 945–961, 2016.
- [87] S. Goes, R. Govers, and P. Vacher, “Shallow mantle temperatures under Europe from P and S wave tomography,” *Journal of Geophysical Research: Solid Earth*, vol. 105, no. B5, pp. 11153–11169, 2000.
- [88] C. Meeßen, *Velocity Conversion. V. v1.0.1*, GFZ Data Services, 2017.
- [89] M. Cacace and A. B. Jacquey, “Flexible parallel implicit modelling of coupled thermal–hydraulic–mechanical processes in fractured rocks,” *Solid Earth*, vol. 8, no. 5, pp. 921–941, 2017.
- [90] A. B. Jacquey and M. Cacace, *GOLEM, a MOOSE-Based Application (Version v1.0)*, Zenodo, 2017.
- [91] M. Feng, S. van der Lee, and M. Assumpção, “Upper mantle structure of South America from joint inversion of waveforms and fundamental mode group velocities of Rayleigh waves,” *Journal of Geophysical Research: Solid Earth*, vol. 112, no. B4, 2007.
- [92] A. J. Schaeffer and S. Lebedev, “Global shear speed structure of the upper mantle and transition zone,” *Geophysical Journal International*, vol. 194, no. 1, pp. 417–449, 2013.
- [93] B. L. N. Kennett, E. R. Engdahl, and R. Buland, “Constraints on seismic velocities in the earth from traveltimes,” *Geophysical Journal International*, vol. 122, no. 1, pp. 108–124, 1995.
- [94] P. Wyllie, “Plate tectonics and magma genesis,” *Geologische Rundschau*, vol. 70, no. 1, pp. 128–153, 1981.
- [95] R. V. Conceição, G. Mallmann, E. Koester, M. Schilling, G. W. Bertotto, and A. Rodriguez-Vargas, “Andean subduction-related mantle xenoliths: isotopic evidence of Sr–Nd decoupling during metasomatism,” *Lithos*, vol. 82, no. 3–4, pp. 273–287, 2005.
- [96] T. L. R. Jalowitzki, R. V. Conceição, Y. Orihashi, G. W. Bertotto, S. Nakai, and M. E. Schilling, “Evolução geoquímica de peridotitos e piroxenitos do Manto Litosférico Subcontinental do vulcão Agua Poca, Terreno Cuyania, Argentina,” *Pesquisas em Geociências*, vol. 37, no. 2, p. 143, 2010.
- [97] S. Maaløe and K. Aoki, “The major element composition of the upper mantle estimated from the composition of lherzolites,” *Contributions to Mineralogy and Petrology*, vol. 63, no. 2, pp. 161–173, 1977.
- [98] F. Cammarano, S. Goes, P. Vacher, and D. Giardini, “Inferring upper-mantle temperatures from seismic velocities,” *Physics of the Earth and Planetary Interiors*, vol. 138, no. 3–4, pp. 197–222, 2003.
- [99] S. V. Sobolev, H. Zeyen, G. Stoll, F. Werling, R. Altherr, and K. Fuchs, “Upper mantle temperatures from teleseismic tomography of French Massif Central including effects of composition, mineral reactions, anharmonicity, anelasticity

- and partial melt," *Earth and Planetary Science Letters*, vol. 139, no. 1-2, pp. 147–163, 1996.
- [100] M. An, D. A. Wiens, Y. Zhao et al., "Temperature, lithosphere-asthenosphere boundary, and heat flux beneath the Antarctic plate inferred from seismic velocities," *Journal of Geophysical Research: Solid Earth*, vol. 120, no. 12, pp. 8720–8742, 2015.
- [101] F. Deschamps, J. Trampert, and R. Snieder, "Anomalies of temperature and iron in the uppermost mantle inferred from gravity data and tomographic models," *Physics of the Earth and Planetary Interiors*, vol. 129, no. 3, pp. 245–264, 2002.
- [102] K. Priestley and D. McKenzie, "The thermal structure of the lithosphere from shear wave velocities," *Earth and Planetary Science Letters*, vol. 244, no. 1–2, pp. 285–301, 2006.
- [103] B. Steinberger and A. R. Calderwood, "Models of large-scale viscous flow in the Earth's mantle with constraints from mineral physics and surface observations," *Geophysical Journal International*, vol. 167, no. 3, pp. 1461–1481, 2006.
- [104] L. Stixrude and C. Lithgow-Bertelloni, "Mineralogy and elasticity of the oceanic upper mantle: origin of the low-velocity zone," *Journal of Geophysical Research*, vol. 110, no. B3, article B03204, 2005.
- [105] C. Meeßen, *Velo DT v1.2 (Version v1.2)*, Zenodo, 2020.
- [106] M. Araneda, G. Asch, K. Bataille et al., "A crustal model along 39° S from a seismic refraction profile-ISSA 2000," *Revista Geológica de Chile*, vol. 30, no. 1, pp. 83–101, 2003.
- [107] E. Contreras-Reyes, I. Grevemeyer, E. R. Flueh, and C. Reichert, "Upper lithospheric structure of the subduction zone offshore of southern Arauco peninsula, Chile, at ~38°S," *Journal of Geophysical Research*, vol. 113, no. B7, article B07303, 2008.
- [108] J. D. Pesicek, E. R. Engdahl, C. H. Thurber, H. R. DeShon, and D. Lange, "Mantle subducting slab structure in the region of the 2010 M8.8 Maule earthquake (30–40°S), Chile," *Geophysical Journal International*, vol. 191, no. 1, pp. 317–324, 2012.
- [109] L. Scarfi and G. Barberi, *New Insights on the Tectonic Structure of the Southern Central Andes–Western Argentina–From Seismic Tomography*, *Geology, Earth and Marine Sciences*, 2019.
- [110] T. M. Brocher, "Empirical relations between elastic Wave-speeds and density in the Earth's crust," *Bulletin of the Seismological Society of America*, vol. 95, no. 6, pp. 2081–2092, 2005.
- [111] N. I. Christensen and W. D. Mooney, "Seismic velocity structure and composition of the continental crust: a global view," *Journal of Geophysical Research: Solid Earth*, vol. 100, no. B6, pp. 9761–9788, 1995.
- [112] P. Alvarado, S. Beck, and G. Zandt, "Crustal structure of the south-central Andes Cordillera and backarc region from regional waveform modelling," *Geophysical Journal International*, vol. 170, no. 2, pp. 858–875, 2007.
- [113] P. Alvarado, M. Pardo, H. Gilbert et al., "Flat-slab subduction and crustal models for the seismically active Sierras Pampeanas region of Argentina," *Backbone of the Americas: Shallow Subduction, Plateau Uplift, and Ridge and Terrane Collision*, vol. 204, 2009.
- [114] J.-B. Ammirati, P. Alvarado, M. Perarnau, M. Saez, and G. Monsalvo, "Crustal structure of the Central Precordillera of San Juan, Argentina (31°S) using teleseismic receiver functions," *Journal of South American Earth Sciences*, vol. 46, pp. 100–109, 2013.
- [115] J.-B. Ammirati, P. Alvarado, and S. Beck, "A lithospheric velocity model for the flat slab region of Argentina from joint inversion of Rayleigh wave phase velocity dispersion and teleseismic receiver functions," *Geophysical Journal International*, vol. 202, no. 1, pp. 224–241, 2015.
- [116] J.-B. Ammirati, A. Venerdini, J. M. Alcacer, P. Alvarado, S. Miranda, and H. Gilbert, "New insights on regional tectonics and basement composition beneath the eastern Sierras Pampeanas (Argentine back-arc region) from seismological and gravity data," *Tectonophysics*, vol. 740–741, pp. 42–52, 2018.
- [117] H. Gilbert, S. Beck, and G. Zandt, "Lithospheric and upper mantle structure of Central Chile and Argentina," *Geophysical Journal International*, vol. 165, no. 1, pp. 383–398, 2006.
- [118] V. Čermák and L. Rybach, "Thermal conductivity and specific heat of minerals and rocks," in *Landolt-Börnstein: Numerical Data and Functional Relationships in Science and Technology, New Series, Group V (Geophysics and Space Research), Volume Ia, (Physical Properties of Rocks)*, G. Angenheister, Ed., pp. 305–343, Springer, Berlin-Heidelberg, 1982.
- [119] D. Hasterok and D. Chapman, "Heat production and geotherms for the continental lithosphere," *Earth and Planetary Science Letters*, vol. 307, no. 1–2, pp. 59–70, 2011.
- [120] L. He, S. Hu, S. Huang et al., "Heat flow study at the Chinese continental scientific drilling site: borehole temperature, thermal conductivity, and radiogenic heat production," *Journal of Geophysical Research*, vol. 113, no. B2, article B02404, 2008.
- [121] M. Vilà, M. Fernández, and I. Jiménez-Munt, "Radiogenic heat production variability of some common lithological groups and its significance to lithospheric thermal modeling," *Tectonophysics*, vol. 490, no. 3–4, pp. 152–164, 2010.
- [122] Y. Xu, T. J. Shankland, S. Linhardt, D. C. Rubie, F. Langenhorst, and K. Klasinski, "Thermal diffusivity and conductivity of olivine, wadsleyite and ringwoodite to 20 GPa and 1373 K," *Physics of the Earth and Planetary Interiors*, vol. 143–144, pp. 321–336, 2004.
- [123] J. Muñoz Sabater, "ERA5-Land monthly averaged data from 1981 to present," *Copernicus Climate Change Service*, vol. 146, 2019.
- [124] S. K. Saxena and G. Shen, "Assessed data on heat capacity, thermal expansion, and compressibility for some oxides and silicates," *Journal of Geophysical Research*, vol. 97, no. B13, p. 19813, 1992.
- [125] H. Berckhemer, W. Kampfmann, E. Aulbach, and H. Schmeling, "Shear modulus and Q of Forsterite and Dunite near partial melting from forced-oscillation experiments," *Physics of the Earth and Planetary Interiors*, vol. 29, no. 1, pp. 30–41, 1982.
- [126] F. Lucazeau, "Analysis and mapping of an updated terrestrial heat flow data set," *Geochemistry, Geophysics, Geosystems*, vol. 20, no. 8, pp. 4001–4024, 2019.
- [127] I. Wada and K. Wang, "Common depth of slab-mantle decoupling: reconciling diversity and uniformity of subduction zones," *Geochemistry, Geophysics, Geosystems*, vol. 10, no. 10, 2009.
- [128] A. F. Holt and C. B. Condit, "Slab temperature evolution over the lifetime of a subduction zone," *Geochemistry, Geophysics, Geosystems*, vol. 22, no. 6, 2021.
- [129] W. Leng and W. Mao, "Geodynamic modeling of thermal structure of subduction zones," *Science China Earth Sciences*, vol. 58, no. 7, pp. 1070–1083, 2015.

- [130] E. M. Syracuse, P. E. van Keken, and G. A. Abers, "The global range of subduction zone thermal models," *Special Issue on Deep Slab and Mantle Dynamics*, vol. 183, no. 1-2, pp. 73–90, 2010.
- [131] K. Priestley and D. McKenzie, "The relationship between shear wave velocity, temperature, attenuation and viscosity in the shallow part of the mantle," *Earth and Planetary Science Letters*, vol. 381, pp. 78–91, 2013.
- [132] H. Sato, I. S. Sacks, and T. Murase, "The use of laboratory velocity data for estimating temperature and partial melt fraction in the low-velocity zone: comparison with heat flow and electrical conductivity studies," *Journal of Geophysical Research: Solid Earth*, vol. 94, no. B5, pp. 5689–5704, 1989.
- [133] H. Schmeling, "Numerical models on the influence of partial melt on elastic, anelastic and electrical properties of rocks. Part II: electrical conductivity," *Physics of the Earth and Planetary Interiors*, vol. 43, no. 2, pp. 123–136, 1986.
- [134] G. M. Mavko, "Velocity and attenuation in partially molten rocks," *Journal of Geophysical Research: Solid Earth*, vol. 85, no. B10, pp. 5173–5189, 1980.
- [135] Y. Takei, "Effects of Partial Melting on Seismic Velocity and Attenuation: A New Insight from Experiments," *Annual Review of Earth and Planetary Sciences*, vol. 45, no. 1, pp. 447–470, 2017.
- [136] A. B. Thompson, "Water in the Earth's upper mantle," *Nature*, vol. 358, no. 6384, pp. 295–302, 1992.
- [137] E. Debayle, T. Bodin, S. Durand, and Y. Ricard, "Seismic evidence for partial melt below tectonic plates," *Nature*, vol. 586, no. 7830, pp. 555–559, 2020.
- [138] M. Tumanian, M. L. Frezzotti, A. Peccerillo, E. Brandmayr, and G. F. Panza, "Thermal structure of the shallow upper mantle beneath Italy and neighbouring areas: Correlation with magmatic activity and geodynamic significance," *Earth-Science Reviews*, vol. 114, no. 3, pp. 369–385, 2012.
- [139] R. D. Hyndman and S. M. Peacock, "Serpentinization of the forearc mantle," *Earth and Planetary Science Letters*, vol. 212, no. 3, pp. 417–432, 2003.
- [140] C. R. Stern, "Active Andean volcanism: its geologic and tectonic setting," *Revista Geológica de Chile*, vol. 31, no. 2, pp. 161–206, 2004.
- [141] P. England, "On shear stresses, temperatures, and the maximum magnitudes of earthquakes at convergent plate boundaries," *Journal of Geophysical Research: Solid Earth*, vol. 123, no. 8, pp. 7165–7202, 2018.
- [142] X. Gao and K. Wang, "Strength of stick-slip and creeping subduction megathrusts from heat flow observations," *Science*, vol. 345, no. 6200, pp. 1038–1041, 2014.
- [143] P. E. van Keken, B. Kiefer, and S. M. Peacock, "High-resolution models of subduction zones: implications for mineral dehydration reactions and the transport of water into the deep mantle," *Geochemistry, Geophysics, Geosystems*, vol. 3, no. 10, 2002.
- [144] P. E. van Keken, I. Wada, G. A. Abers, B. R. Hacker, and K. Wang, "Mafic high-pressure rocks are preferentially exhumed from warm subduction settings," *Geochemistry, Geophysics, Geosystems*, vol. 19, no. 9, pp. 2934–2961, 2018.
- [145] M. J. Kohn, A. E. Castro, B. C. Kerswell, C. R. Ranero, and F. S. Spear, "Shear heating reconciles thermal models with the metamorphic rock record of subduction," *Proceedings of the National Academy of Sciences*, vol. 115, no. 46, pp. 11706–11711, 2018.
- [146] D. McKenzie, J. Jackson, and K. Priestley, "Thermal structure of oceanic and continental lithosphere," *Earth and Planetary Science Letters*, vol. 233, no. 3-4, pp. 337–349, 2005.
- [147] F. Lucazeau and S. Le Douaran, "The blanketing effect of sediments in basins formed by extension: a numerical model. Application to the Gulf of Lion and Viking graben," *Earth and Planetary Science Letters*, vol. 74, no. 1, pp. 92–102, 1985.
- [148] M. Wangen, "The blanketing effect in sedimentary basins," *Basin Research*, vol. 7, no. 4, pp. 283–298, 1995.
- [149] F. J. Calixto, E. Sandvol, S. Kay et al., "Velocity structure beneath the southern Puna plateau: evidence for delamination: velocity structure in the Southern Puna," *Geochemistry, Geophysics, Geosystems*, vol. 14, no. 10, pp. 4292–4305, 2013.
- [150] Y. Gao, F. Tilmann, D. van Herwaarden et al., "Full Waveform Inversion beneath the Central Andes: Insight into the Dehydration of the Nazca Slab and Delamination of the Back-Arc Lithosphere," *Journal of Geophysical Research: Solid Earth*, vol. 126, no. 7, 2021.
- [151] S. M. Kay, B. Coira, and J. Viramonte, "Young mafic back arc volcanic rocks as indicators of continental lithospheric delamination beneath the Argentine Puna Plateau, central Andes," *Journal of Geophysical Research: Solid Earth*, vol. 99, no. B12, pp. 24323–24339, 1994.
- [152] B. Schurr, A. Rietbrock, G. Asch, R. Kind, and O. Oncken, "Evidence for lithospheric detachment in the central Andes from local earthquake tomography," *Tectonophysics*, vol. 415, no. 1-4, pp. 203–223, 2006.
- [153] L. Chen, X. Song, T. V. Gerya, T. Xu, and Y. Chen, "Crustal melting beneath orogenic plateaus: insights from 3-D thermo-mechanical modeling," *Tectonophysics*, vol. 761, pp. 1–15, 2019.
- [154] K. P. Furlong and D. S. Chapman, "Heat flow, heat generation, and the thermal state of the lithosphere," *Annual Review of Earth and Planetary Sciences*, vol. 41, no. 1, pp. 385–410, 2013.
- [155] M. Gerbault, J. Cembrano, C. Mpodozis, M. Farias, and M. Pardo, "Continental margin deformation along the Andean subduction zone: thermo-mechanical models," *Physics of the Earth and Planetary Interiors*, vol. 177, no. 3-4, pp. 180–205, 2009.
- [156] C. Jaupart, J.-C. Mareschal, and L. Iarotsky, "Radiogenic heat production in the continental crust," *Lithos*, vol. 262, pp. 398–427, 2016.
- [157] S. C. Penniston-Dorland, M. J. Kohn, and C. E. Manning, "The global range of subduction zone thermal structures from exhumed blueschists and eclogites: rocks are hotter than models," *Earth and Planetary Science Letters*, vol. 428, pp. 243–254, 2015.
- [158] L. Kaislaniemi, J. Hunen, and P. Bouilhol, "Lithosphere Destabilization by Melt Weakening and Crust-Mantle Interactions: Implications for Generation of Granite-Migmatite Belts," *Lithosphere Destabilization by Melt Weakening and Crust-Mantle Interactions: Implications for Generation of Granite-Migmatite Belts*, vol. 37, no. 9, pp. 3102–3116, 2018.
- [159] R. D. Hyndman, C. A. Currie, and S. P. Mazzotti, "Subduction zone backarcs, mobile belts, and orogenic heat," *GSA Today*, vol. 15, no. 2, p. 4, 2005.
- [160] W. J. Collins, "Hot orogens, tectonic switching, and creation of continental crust," *Geology*, vol. 30, no. 6, pp. 535–538, 2002.

- [161] A. B. Thompson, K. Schulmann, J. Jezek, and V. Tolar, "Thermally softened continental extensional zones (arcs and rifts) as precursors to thickened orogenic belts," *Tectonophysics*, vol. 332, no. 1-2, pp. 115–141, 2001.
- [162] R. Porter, H. Gilbert, G. Zandt et al., "Shear wave velocities in the Pampean flat-slab region from Rayleigh wave tomography: implications for slab and upper mantle hydration," *Journal of Geophysical Research: Solid Earth*, vol. 117, no. B11, 2012.
- [163] P. E. van Keken, S. Kita, and J. Nakajima, "Thermal structure and intermediate-depth seismicity in the Tohoku-Hokkaido subduction zones," *Solid Earth*, vol. 3, no. 2, pp. 355–364, 2012.
- [164] D. A. Oleskevich, R. D. Hyndman, and K. Wang, "The updip and downdip limits to great subduction earthquakes: thermal and structural models of Cascadia, south Alaska, SW Japan, and Chile," *Journal of Geophysical Research: Solid Earth*, vol. 104, no. B7, pp. 14965–14991, 1999.
- [165] I. Artemieva, *Lithosphere: An Interdisciplinary Approach*, Cambridge University Press, 2011.
- [166] P. Deshayes, *Velocity and Attenuation Tomography of the Subduction Zone in Central Chile-Western Argentina (29°S-34°S) from Local Seismic Data: Contribution to the Mineralogical Composition Study*, Université Nice Sophia Antipolis, 2008, <https://tel.archives-ouvertes.fr/tel-00360063>.
- [167] D. W. Rees Jones, R. F. Katz, M. Tian, and J. F. Rudge, "Thermal impact of magmatism in subduction zones," *Earth and Planetary Science Letters*, vol. 481, pp. 73–79, 2018.
- [168] E. Burov, "Coupled lithosphere-surface processes in collision context," in *Thrust Belts and Foreland Basins*, pp. 3–40, Springer, 2007.
- [169] S. Nacif, M. Lupari, E. G. Triep et al., "Change in the pattern of crustal seismicity at the Southern Central Andes from a local seismic network," *Tectonophysics*, vol. 708, pp. 56–69, 2017.
- [170] A. Tassara and G. Yáñez, "Relación entre el espesor elástico de la litosfera y la segmentación tectónica del margen andino (15-47°S)," *Andean Geology*, vol. 30, no. 2, pp. 159–186, 2003.
- [171] E. Burov and M. Diament, "The effective elastic thickness (T_e) of continental lithosphere: what does it really mean?," *Journal of Geophysical Research*, vol. 100, no. B3, pp. 3905–3927, 1995.
- [172] A. B. Watts and E. B. Burov, "Lithospheric strength and its relationship to the elastic and seismogenic layer thickness," *Earth and Planetary Science Letters*, vol. 213, no. 1-2, pp. 113–131, 2003.
- [173] F. Ibarra, S. Liu, C. Meeßen et al., "3D data-derived lithospheric structure of the Central Andes and its implications for deformation: insights from gravity and geodynamic modelling," *Tectonophysics*, vol. 766, pp. 453–468, 2019.
- [174] C. Meeßen, *The Thermal and Rheological State of the Northern Argentinian Foreland Basins*, [Ph.D. thesis], Universität Potsdam, 2019.
- [175] B. K. Horton, "Sedimentary record of Andean mountain building," *Earth-Science Reviews*, vol. 178, pp. 279–309, 2018.
- [176] J. Martinod, M. Gérard, L. Husson, and V. Regard, "Widening of the Andes: an interplay between subduction dynamics and crustal wedge tectonics," *Earth-Science Reviews*, vol. 204, article 103170, 2020.
- [177] G. E. Hilley, P. M. Blisniuk, and M. R. Strecker, "Mechanics and erosion of basement-cored uplift provinces," *Journal of Geophysical Research: Solid Earth*, vol. 110, no. B12, 2005.
- [178] F. Hongn, C. Papadel, J. Powell, I. Petrinovic, R. Mon, and V. Deraco, "Middle Eocene deformation and sedimentation in the Puna-Eastern Cordillera transition (23°-26°S): control by preexisting heterogeneities on the pattern of initial Andean shortening," *Geology*, vol. 35, no. 3, pp. 271–274, 2007.
- [179] F. Hongn, R. Mon, I. Petrinovic, C. del Papa, and J. Powell, "Inversión y reactivación tectónicas cretácico-cenozoicas en el noroeste argentino: influencia de las heterogeneidades del basamento Neoproterozoico-Paleozoico inferior," *Revista de la Asociación Geológica Argentina*, vol. 66, no. 1–2, pp. 38–53, 2010.
- [180] D. M. Pearson, P. Kapp, P. G. DeCelles et al., "Influence of pre-Andean crustal structure on Cenozoic thrust belt kinematics and shortening magnitude: Northwestern Argentina," *Geosphere*, vol. 9, no. 6, pp. 1766–1782, 2013.
- [181] S. Zapata, E. R. Sobel, C. Del Papa, and J. Glodny, "Upper plate controls on the formation of broken foreland basins in the Andean Retroarc between 26°S and 28°S: from cretaceous rifting to Paleogene and Miocene broken foreland basins," *Geochemistry, Geophysics, Geosystems*, vol. 21, no. 7, 2020.
- [182] V. A. Ramos and A. Folguera, "Andean flat-slab subduction through time," *Geological Society, London, Special Publications*, vol. 327, no. 1, pp. 31–54, 2009.